

REPORT DOCUMENTATION PAGE			Form Approved OMB No. 0704-0188	
Public reporting burden for this collection of information is estimated to average 1 hour per response, including the time for reviewing instructions, searching existing data sources, gathering and maintaining the data needed, and completing and reviewing the collection of information. Send comments regarding this burden estimate or any other aspect of this collection of information, including suggestions for reducing this burden, to Washington Headquarters Services, Directorate for Information Operations and Reports, 1215 Jefferson Davis Highway, Suite 1204, Arlington, VA 22202-4302, and to the Office of Management and Budget, Paperwork Reduction Project (0704-0188), Washington, DC 20503.				
1. AGENCY USE ONLY (Leave blank)		2. REPORT DATE		3. REPORT TYPE AND DATES COVERED
		10 Jun.02		THESIS
4. TITLE AND SUBTITLE				5. FUNDING NUMBERS
VISCIOUS DRAG MEASUREMENT AND ITS APPLICATION TO BASE DRAG REDUCTION				
6. AUTHOR(S)				8. PERFORMING ORGANIZATION REPORT NUMBER
2D LT DECKER ROBERT K				
7. PERFORMING ORGANIZATION NAME(S) AND ADDRESS(ES)				10. SPONSORING/MONITORING AGENCY REPORT NUMBER
UNIVERSITY OF WYOMING				
9. SPONSORING/MONITORING AGENCY NAME(S) AND ADDRESS(ES)				12b. DISTRIBUTION CODE
THE DEPARTMENT OF THE AIR FORCE AFIT/CIA, BLDG 125 2950 P STREET WPAFB OH 45433				
11. SUPPLEMENTARY NOTES				
12a. DISTRIBUTION AVAILABILITY STATEMENT				13. ABSTRACT (Maximum 200 words)
Unlimited distribution In Accordance With AFI 35-205/AFIT Sup 1				
14. SUBJECT TERMS				
15. NUMBER OF PAGES				16. PRICE CODE
86				
17. SECURITY CLASSIFICATION OF REPORT	18. SECURITY CLASSIFICATION OF THIS PAGE	19. SECURITY CLASSIFICATION OF ABSTRACT	20. LIMITATION OF ABSTRACT	

20020702 029

Decker, Robert K., Viscous Drag Measurement and Its Application to Base Drag Reduction, M.S., Department of Mechanical Engineering, May, 2002.

In this study two important topics have been investigated. First, a new automation procedure has been developed to detect fringe patterns in oil-film interferograms. The procedure combines a windowed Fourier transform and a cross correlation technique to determine regions where fringes are likely to reside. The cross correlation of a single cycle cosine function and the original intensity produce a filtered result that isolates the information being sought. The automation procedure is able to capture approximately 75% of the fringes in an image but additional refining of the technique could increase this percentage. Second, the effect of viscous fore-body drag on base drag has been investigated on a 2-D ramp model. Measurements made during the study include oil-film interferometry and hot-wire anemometry for viscous fore-body drag, and pressure measurements on the fore-body and base for fore-body and base drag. The results of this investigation show that an increase in viscous fore-body drag has very little effect on base drag, which contrasts previous studies where increases in viscous fore-body drag tended to decrease base drag. This means that a simple jet pumping mechanism is not the sole effect responsible for base drag reduction in this type of geometry. Hot-wire measurements in the wake of the model show that the flow in the base region is devoid of a dominant shedding frequency. It may be possible that the boundary layer somehow affects the vortex shedding mechanism but further investigations would be necessary to demonstrate that this is true.

Author: Robert K. Decker  
Title: Viscous Drag Measurement and its Application to Base Drag Reduction  
Rank: 2dLt  
Service: USAF  
Date: 2002  
Pages: 87  
Degree: Master of Science in Mechanical Engineering  
Institution: University of Wyoming

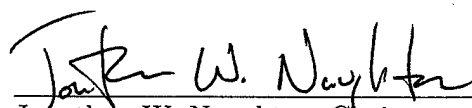
## References

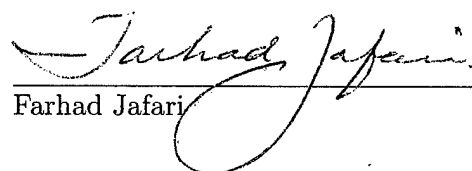
- OVERFLOW User's Manual*, February 1998. Version 1.8.
- Matlab Image Processing Toolkit*, third edition, June 2001.
- J. Bendat and A. Piersol. *Random Data: Analysis and Measurement Procedures*. John Wiley & Sons, New York, NY, 1986.
- L. Cattafesta III and J. Moore. Review and Application of Non-topographic Photogrammetry to Quantitative Flow Visualization. AIAA Paper 96-2180, June 1996.
- L. Clancy. *Aerodynamics*. Halsted Press, 1975.
- H. Coleman and W. Steele Jr. *Experimentation and Uncertainty Analysis for Engineers*. John Wiley and Sons, 1st edition, 1989.
- R. Decker and J. Naughton. Improved Fringe Imaging Skin Friction Analysis Using Automated Fringe Identification. AIAA Paper 2001-0557, January 2001.
- R. Decker, J. Naughton, and F. Jafari. Automatic Fringe Detection for Oil Film Interferometric Skin-Friction Measurement. In I. Grant and G. Carlomagno, editors, *Proceedings of the 9th International Symposium on Flow Visualization*, 2000. (on CD ROM, ISBN 0 9533991 1 7).
- D. Driver. Application of Oil Film Interferometry Skin-Friction to Large Wind Tunnels. In *81st AGARD Fluid Dynamics Panel Meeting & Symposium, Sept. 22-25, Seattle WA*, 1997.
- T. Garrison and M. Ackman. Development of a Global Interferometer Skin-Friction Meter. *AIAA Journal*, 36(1):62-68, January 1998.
- S. Hoerner. *Fluid Dynamic Drag*. Self-published, 1965.
- P. Krogstad and R. Antonia. Surface Roughness Effects in Turbulent Boundary Layers. *Experiments in Fluids*, 27:450-460, 1999.
- H. Kurzweg. Interrelationship Between Boundary Layer and Base Pressure. *Journal of the Aeronautical Sciences*, pages 743-748, 1951.
- K. Levenberg. A Method for the Solution of Certain Problems in Least Squares. *Quarterly of Applied Mathematics*, 2:164-168, 1944.
- W. Li. Characteristics of Turbulent Boundary Layers on Rough Surfaces with Favorable Pressure Gradients. Master's thesis, University of Wyoming, Laramie, WY, August 2001.

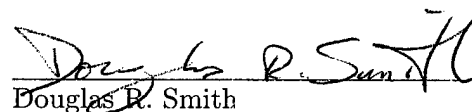
- F. White. *Viscous Fluid Flow*. McGraw-Hill, 2nd edition, 1991.
- S. Whitmore and T. Moes. A Base Drag Reduction Experiment on the X-33 Linear Aerospike SR-71 Experiment (LASRE) Flight Program. AIAA Paper 99-0277, January 1999.
- S. Whitmore, S. Sprague, and J. Naughton. Wind-tunnel Investigations of Blunt-body Drag Reduction Using Forebody Surface Roughness. AIAA Paper 2001-0252, January 2001.
- G. Zilliac. Further Developments of the Fringe-Imaging Skin Friction Technique. Technical report, NASA TM 110425, December 1996.
- G. Zilliac. The Fringe-Imaging Skin Friction Technique PC Application User's Manual. Technical report, NASA TM 1999-208794, 1999.

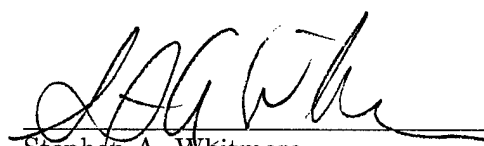
To The Graduate School:

The members of the Committee approve the thesis of Robert K. Decker presented on December 19, 2001.

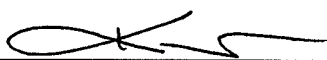
  
Jonathan W. Naughton, Chairman

  
Farhad Jafari

  
Douglas R. Smith

  
Stephen A. Whitmore

APPROVED:

  
Demitris A. Kouris, Head, Department of Mechanical Engineering

\_\_\_\_\_  
Stephen E. Williams, Dean, The Graduate School

VISCOUS DRAG MEASUREMENT AND ITS APPLICATION TO BASE DRAG  
REDUCTION

by  
Robert K. Decker

A thesis submitted to The Department of Mechanical Engineering  
and The Graduate School of The University of Wyoming  
in partial fulfillment of the requirements  
for the degree of

MASTER OF SCIENCE  
in  
MECHANICAL ENGINEERING

Laramie, Wyoming  
May, 2002

© Copyright by Robert K. Decker, 2002

# Table of Contents

<b>Table of Contents</b>	<b>v</b>
<b>List of Tables</b>	<b>vi</b>
<b>List of Figures</b>	<b>vii</b>
<b>Acknowledgements</b>	<b>xi</b>
<b>1 Background</b>	<b>1</b>
1.1 Introduction and Motivation . . . . .	1
1.2 Literature Review . . . . .	5
1.2.1 Splitter Plates . . . . .	5
1.2.2 Modification of Boundary Layer State . . . . .	6
<b>2 Experimental Setup and Instrumentation</b>	<b>9</b>
2.1 Overview . . . . .	9
2.2 Ramp Model . . . . .	9
2.3 Ambient and Reference Conditions . . . . .	13
2.4 Oil-film Interferometry . . . . .	13
2.4.1 Oil Calibration . . . . .	14
2.4.2 Image Acquisition System . . . . .	15
2.4.3 Data/Image Acquisition Software . . . . .	18
2.4.4 Interferogram Analysis . . . . .	20
2.5 Hot-Wire Anemometry . . . . .	26
2.6 Pressure Measurement . . . . .	27
2.7 Test Cases . . . . .	28
<b>3 Automated Interference Fringe Pattern Recognition</b>	<b>29</b>
3.1 Introduction . . . . .	29
3.2 Oil Film Interferometry for Skin Friction Measurement . . . . .	30



3.3	Theoretical Background . . . . .	33
3.4	Fringe-Detection Method . . . . .	34
3.4.1	Filters Based on Dominant Principal Component Waveforms . . . . .	35
3.4.2	Cosine Interrogation Fringe . . . . .	36
3.5	Results . . . . .	39
3.6	Conclusions . . . . .	43
<b>4</b>	<b>Modification of Base Pressure Through Boundary Layer Manipulation</b>	<b>45</b>
4.1	Nomenclature . . . . .	45
4.2	Introduction . . . . .	47
4.3	Experimental Approach . . . . .	50
4.3.1	2' $\times$ 2' Subsonic Wind Tunnel . . . . .	50
4.3.2	Ramp Model . . . . .	50
4.3.3	Surface Roughness . . . . .	52
4.3.4	Test Cases . . . . .	53
4.4	Instrumentation . . . . .	54
4.4.1	Oil-Film Interferometry . . . . .	55
4.4.2	Hot-Wire Anemometry . . . . .	56
4.5	Data Corrections . . . . .	59
4.5.1	Simulation . . . . .	59
4.5.2	Free-Stream Conditions . . . . .	60
4.5.3	Blockage Effect . . . . .	61
4.6	Results . . . . .	62
4.6.1	Assessment of $C_f$ Measurement Techniques . . . . .	62
4.6.2	Integral Boundary Layer Properties . . . . .	62
4.6.3	Skin-Friction Results . . . . .	63
4.6.4	Fore-Body Pressure Results . . . . .	64
4.6.5	Base Pressure Results . . . . .	66
4.6.6	Integrated Results . . . . .	67
4.6.7	Wake Measurements . . . . .	70
4.6.8	Discussion . . . . .	70
4.7	Conclusion . . . . .	72
<b>5</b>	<b>Conclusions</b>	<b>74</b>
	<b>Bibliography</b>	<b>76</b>
<b>A</b>	<b>Uncertainty Analysis</b>	<b>80</b>
A.1	Density Uncertainty . . . . .	80
A.2	Pitot Static Pressure Uncertainty . . . . .	81

A.3	Free-Stream Velocity Uncertainty . . . . .	81
A.4	Base Pressure Uncertainty . . . . .	82
A.5	Pressure Coefficient Uncertainty . . . . .	82
A.6	Skin Friction Uncertainty . . . . .	83
A.6.1	Hot-Wire Anemometry . . . . .	83
<b>B</b>	<b>Detailed Derivations</b>	<b>85</b>
B.1	Oil Calibration . . . . .	85

# List of Tables

2.1	Details of sand grains used to produce roughness. Here $k$ is equivalent to the sand grain diameter $D_s$ . . . . .	11
2.2	Properties of Dow Corning 200 fluid used for oil-film interferometry measurements. . . . .	14
2.3	Oil-film interferometry image acquisition system parts list. . . . .	18
4.1	Sand grain sizes used to produce surface roughness. . . . .	53
4.2	Range of surface roughness in wall units for two ramp configurations. . . . .	54
4.3	Test cases: HWA - hot-wire anemometry, OFI - oil-film interferometry, BP - base pressure, and FB - fore-body pressure. The symbols after each case listing correspond to those in the graphs. . . . .	55
4.4	Integral boundary layer properties near the trailing edge of the ramp for various test conditions. Used with permission from [15]. . . . .	64
A.1	Base pressure measurement uncertainty. . . . .	83
A.2	Pressure coefficient uncertainty. . . . .	84
B.1	Properties measured during viscosity calibration. . . . .	86

# List of Figures

1.1	Representation of reusable launch vehicle gliding in atmosphere after reentry. . . . .	2
1.2	Effect of boundary layer state (thickness) on momentum deficit: (a) thin boundary layer with greater momentum deficit and (b) thicker boundary layer with decreased momentum deficit. . . . .	4
2.1	Schematic of ramp model with interchangeable plates. . . . .	10
2.2	Image of sand grains fixed to plate surface: (a) small, (b) medium, and (c) large sand. One ruler division is .794mm. . . . .	12
2.3	Roughness height in wall variables: (a) 3 degree ramp with $U_{\infty}=50$ m/s and (b) 5 degree ramp with $U_{\infty}=40$ m/s. See Table 4.3 for symbol definitions. . . . .	13
2.4	Schematic of "in-line" oil-film interferometry image acquisition system.	16
2.5	"In-line" oil-film interferometry image acquisition system. . . . .	17
2.6	Mercury grid light source used with oil-film interferometry image acquisition system. . . . .	19
2.7	Interferogram with analysis line overlaid. Note the crosses in the figure that are used for registration purposes. . . . .	21
2.8	Steps of fringe analysis to determine skin friction coefficient: (a) Intensity along the line shown in Fig. 2.7; (b) Interrogation fringe; (c) cross-correlation coefficient; (d) oil-film height; and (e) skin friction coefficient. . . . .	23

2.9	Auto-spectral density of the intensity signal in Fig. 2.8(a). Note the peak located away from zero frequency. . . . .	24
2.10	Streamline-based coordinate system used for oil-film interferogram analysis. . . . .	25
3.1	Interference fringes produced by Fizeau Interferometry: (a) constructive interference produces bright bands, whereas (b) destructive interference produces dark bands. The interference fringes move as the oil height changes due to the aerodynamic shear stress $\tau$ acting on the oil film. This figure is used with permission from reference [20]. . . . .	31
3.2	Interferogram resulting from oil drops placed at various location on a wing surface. This image is courtesy of David Driver, NASA-Ames Research Center. . . . .	32
3.3	One-dimensional example of fringe detection: (a) portion of original image indicating windowed area; (b) intensity distribution within window; (c) autospectral density of intensity distribution; (d) zero-mean, padded intensity distribution; (e) interrogation fringe constructed from peak frequency in autospectral density; (f) cross-correlation coefficient with peaks and valleys identified. Note that the numbers in (f) correspond to the peaks and valleys of the correlation coefficient, which correspond to the peaks and valleys in the interference pattern indicated in (b) and (d). . . . .	37
3.4	Two-dimensional fringe-detection method: (a) windowed area containing a fringe and the location of the peaks and valleys indicated by filled symbols; (b) interrogation fringe, (c) cross-correlation coefficient, (d) cross-correlation coefficient with iso-contours overlaid, (e) cross-correlation coefficient with minima and maxima indicated by symbols and contours used to reject additional peak points shown. . . . .	41

3.5	Two-dimensional fringe detection applied to an experimental image. The white stars correspond to valleys in the fringe pattern, whereas the black stars correspond to peaks: (a) $ \rho_{I,IF}  > 0.30$ for a peak or valley, and (b) $ \rho_{I,IF}  > 0.25$ for a peak or valley. . . . .	43
4.1	Effect of viscous fore-body drag on base drag: (a) relationship between viscous fore-body drag and base drag, (b) "drag bucket" concept. . .	48
4.2	View of ramp model: (a) isometric view of assembled model and (b) base area of ramp model. . . . .	51
4.3	Side view of ramp model. . . . .	52
4.4	Side profile of oil-film "wedge". Used with permission from [19]. . . .	56
4.5	Example thin-oil-film interferogram. This interferogram was produced using the oil-drop approach. . . . .	57
4.6	Boundary layer profiles at 791 mm from the leading edge for four different roughness values. See Table 4.3 for symbol definitions. . . . .	58
4.7	Skin-friction coefficient for smooth flat plate, $U_\infty=50$ m/s. Used with permission from [15]. . . . .	63
4.8	Skin-friction coefficient: (a) 3 degree ramp with $U_\infty=47.4$ m/s and (b) 5 degree ramp with $U_\infty=40.7$ m/s. See Table 4.3 for symbol definitions. Rough surface data used with permission from [15]. . . . .	65
4.9	Fore-body pressure coefficient for the ramp cases. See Table 4.3 for symbol definitions. . . . .	66
4.10	Coefficient of pressure for ramp base area: $3^\circ$ ramp at $U_\infty = 47.4$ m/s and $5^\circ$ ramp at $U_\infty = 40.7$ m/s. See Table 4.3 for symbol definitions. . . . .	67
4.11	Effect of viscous fore-body drag on base drag. See Table 4.3 for symbol definitions. The solid line represents Hoerner's 2-D surface imperfections (i.e. sheet metal junctions) curve and the dotted line represents Hoerner's 3-D curve. . . . .	68

4.12	Effect of viscous fore-body drag on total pressure drag. See Table 4.3 for symbol definitions. The solid line represents Hoerner's 2-D surface imperfections (i.e. sheet metal junctions) curve and the dotted line represents Hoerner's 3-D curve. . . . .	69
4.13	Auto-spectral density of fluctuating velocities measured at a location $x/h = 0.59$ behind the $3^\circ$ ramp at $U_{\text{ref}} = 47$ m/s. . . . .	71

**THE VIEWS EXPRESSED IN THIS ARTICLE  
ARE THOSE OF THE AUTHOR AND DO NOT  
REFLECT THE OFFICIAL POLICY OR  
POSITION OF THE UNITED STATES,  
DEPARTMENT OF DEFENSE, OR THE U.S.  
GOVERNMENT**



# Chapter 1

## Background

### 1.1 Introduction and Motivation

Two types of drag can occur on bodies moving through a fluid: viscous and pressure drag. Viscous drag results from a shearing stress at the surface of the body, whereas pressure drag arises from pressure gradients around the body. Base drag is a special subset of pressure drag that is due to large separated regions on the aft side of a body.

Although the study of base drag and its reduction is important for many fluid flow applications, the primary motivation for this study is the reduction of base drag on the next generation of reusable launch vehicles. These vehicles are of interest because they tend to have large base area to wetted fore-body area ratios. An example of such a configuration is the experimental reusable launch vehicle X-33, which requires a large base area to accommodate the linear aerospike engines it employs. Even though the large base area is necessary for the vehicle design, it also means that the vehicle is dominated by base drag effects as it flies through the atmosphere on reentry (base drag does not dominate during launch conditions since the engines are running).

The increased magnitude of base drag has an adverse effect on the lift-to-drag ratio ( $L/D$ ). Fig. 1.1 depicts a vehicle gliding through the atmosphere. Two important

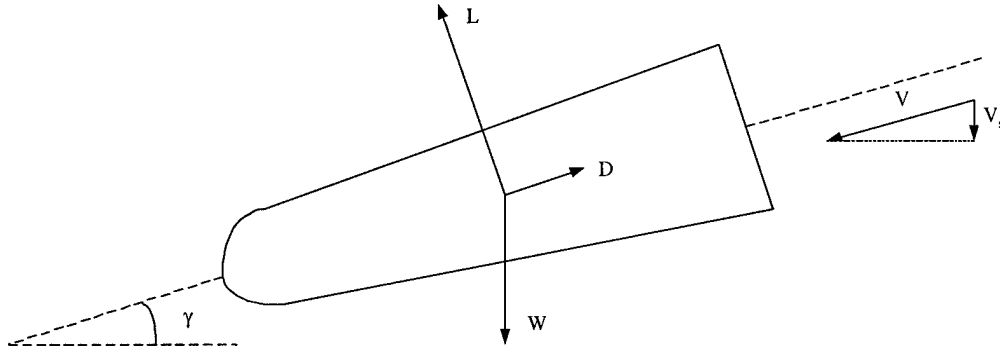


Figure 1.1: Representation of reusable launch vehicle gliding in atmosphere after reentry.

quantities that govern unpowered flight are the glide slope angle  $\gamma$

$$\cot \gamma = \frac{L}{D}, \quad (1.1)$$

and the rate of descent  $V_s$

$$V_s = \sqrt{\frac{2W}{\rho S}} \frac{C_D}{(C_L^2 + C_D^2)^{3/4}}, \quad (1.2)$$

where  $L$  is the vehicle lift,  $D$  is the vehicle drag,  $W$  is the vehicle weight,  $\rho$  is the air density,  $S$  is the vehicle planform area,  $C_D \equiv (2D)/(\rho V^2 S)$  is the drag coefficient, and  $C_L \equiv (2L)/(\rho V^2 S)$  is the lift coefficient (from Clancy [5]). From equations 1.1 and 1.2, it can be shown that, as the base drag increases,  $L/D$  decreases, which translates directly into an increase in glide slope angle, as well as an increase in descent velocity. An increase in glide slope angle directly corresponds to a decrease in the cross range and down range distances. Since these vehicles travel along a specific path in orbit, limiting the cross and down ranges could mean that certain landing sites would be unavailable upon reentry.

Fortunately it appears that earlier studies (see, for example, Hoerner [11] and Whitmore *et al.* [35]) indicate that it is possible to reduce the base drag on these types of vehicles. Hoerner [11] has determined relationships between the viscous forebody drag and base drag from several bluff bodied vehicle configurations as shown

in Fig. 4.1(a). It should be noted from this graph that, for certain fore-body drag values, an increase in the viscous fore-body drag decreases the base drag. Using these relationships, it is possible to determine an operating point where the overall drag of the vehicle is a minimum. If the sum of the viscous fore-body drag and the base drag is assumed to account for the majority of the drag on the vehicle, their sum is approximately the total drag on the vehicle. A plot of the total drag versus the viscous fore-body drag, shown in Fig. 4.1(b), indicates the existence of an ideal operating point where the overall drag of the vehicle is at a minimum. This minimum drag point at a specific fore-body drag value has led to the description of this curve as a “drag bucket” (see reference [23] for further discussion of the “drag bucket” concept).

Hoerner has postulated that the “drag bucket” occurs because, as the boundary layer thickens due to the increase in viscous fore-body drag, lower momentum fluid in the base area is further isolated from high momentum fluid in the free-stream. By reducing the amount of base fluid reaccelerated by the free-stream, the momentum transferred to the base fluid is reduced resulting in a decrease in the overall drag. Fig. 1.2(a) shows the case with low viscous fore-body drag where the boundary layer is relatively thin and the high momentum fluid in the free-stream is allowed to mix with a relatively large amount of the fluid in the base area, causing a greater loss in momentum. The high loss of momentum causes a lower pressure in the base and thus a higher base drag. Correspondingly, Fig. 1.2(b) shows the case with high viscous fore-body drag, which exhibits a thicker boundary layer, a decrease in the amount of free-stream fluid that mixes with the fluid in the base area, and thus a lower momentum deficit. As a result, the base pressure is higher and there is a decrease in base drag.

In order to demonstrate the “drag bucket” concept, the current study investigated the relationship between viscous fore-body drag and base drag on a simple two-dimensional ramp model. Two base heights and different levels of viscous fore-body drag were investigated to compare with Hoerner’s relationship. The results will be

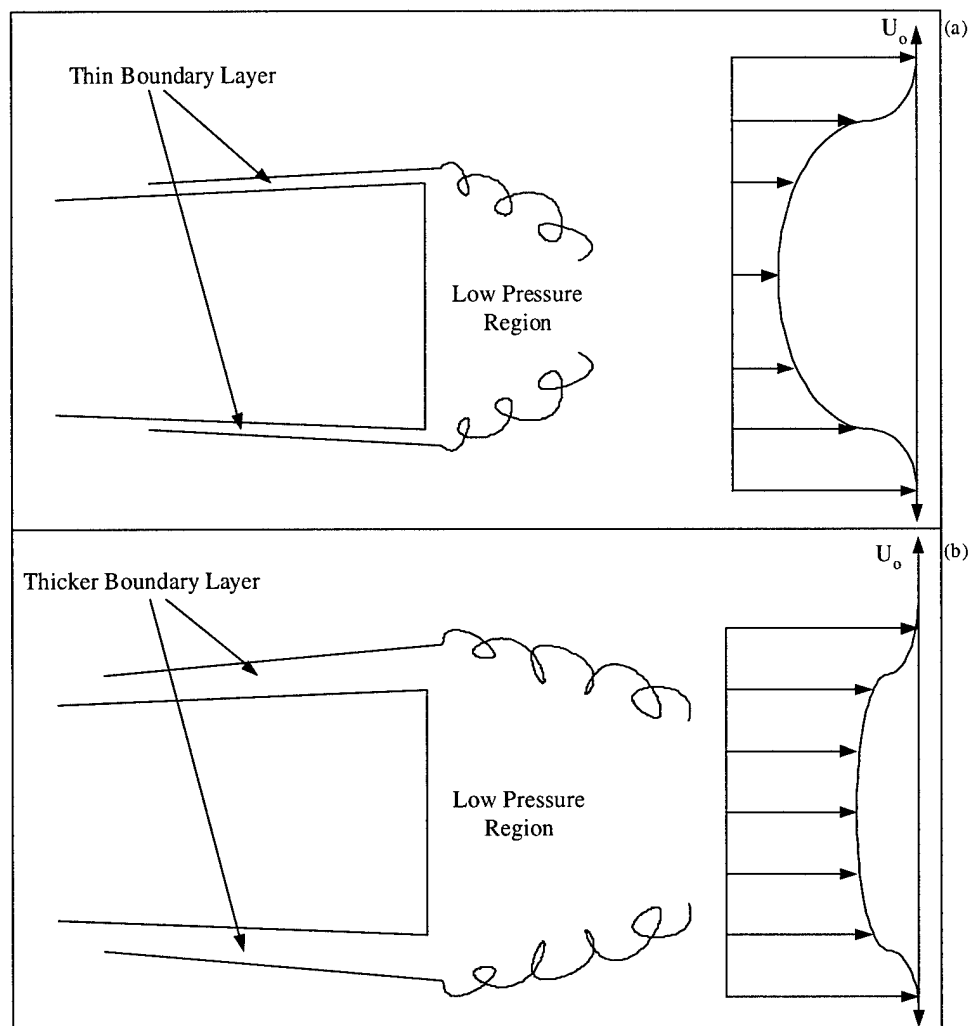


Figure 1.2: Effect of boundary layer state (thickness) on momentum deficit: (a) thin boundary layer with greater momentum deficit and (b) thicker boundary layer with decreased momentum deficit.

used to determine if modifications of viscous fore-body drag could be employed to reduce the overall drag on reusable launch vehicles.

This thesis is organized as follows. First, a review of previous base drag reduction studies is presented and is related to the current study. Chapter 2 then explains the experimental facilities and instrumentation used for the study. Chapter 3 presents a new method for detecting fringe patterns for use with the oil-film interferometry techniques used in this study. Chapter 4 contains the important results determined from the study. Chapter 5 then presents the conclusions of the study with recommendations for future work. Appendix A presents the uncertainty of the measurements used in the study and Appendix B provides detailed derivations of some relationships used over the course of the study.

## 1.2 Literature Review

A brief overview of base drag is presented here. The papers are presented by topic to provide the reader with a perspective on the different methods of reducing base drag.

Various methods for base drag reduction have been studied including splitter plates, base bleed, and trailing edge treatments. Other studies have tried to characterize the boundary layer to explain its effect on base pressure. While all of these studies are relevant to base drag and its reduction, this literature review focuses on splitter plates and boundary layer effects. For a more detailed review base drag reduction methods, see Tanner [31].

### 1.2.1 Splitter Plates

In a report by Roshko [21], vortex shedding frequency and base pressure on two-dimensional bluff bodies were studied. The study focused entirely on incompressible subsonic flow. Roshko theorized that the low pressure on the base area was caused largely by the interactions of the vortices shed from the body. To validate this conclusion, the vortex interactions were impaired using a splitter plate. Roshko thought

that impairing the vortex dynamics would have a direct effect on the base pressure. The first study was on a circular cylinder with a long splitter plate ( $l/d = 4.5$ ). The Reynolds number based on the cylinder diameter for this flow was 14,500. This study concluded that the base drag of the cylinder fitted with the splitter plate was 37% lower than the cylinder without the splitter plate. Next, Roshko studied flow past a flat plate perpendicular to the free-stream direction. In this case, the splitter plate reduced the base drag by 26% over the case without the splitter plate. The results showed that a splitter plate inhibited formation of the periodic vortices with a corresponding increase in the base pressure (and thus a reduction in the base drag). From these results, Roshko drew the conclusion that “it is clear that, without the splitter plate, the periodic formation of vortices is an essential part of the base pressure mechanism.”

Tanner [31] reviewed his own work with several wedges, with and without splitter plates, under nominally two-dimensional test conditions. From these tests, it was concluded that a splitter plate of sufficient length (typically four or five times the body thickness) wholly suppressed the periodic vortex shedding from the body and the base flow could be considered “steady” (it should be noted that “steady” base flow is usually highly turbulent). These “steady” base area flows exhibited the greatest reduction in base drag, and thus it was concluded that “a periodic base flow should be made steady to reduce base drag.”

### 1.2.2 Modification of Boundary Layer State

Kurzweg [13] considered the results of base pressure measurements on 5-cm diameter cylindrical bodies over a Mach number range of 1.5 to 5.0. Kurzweg suggested that the results of the base pressure measurements could be separated into two distinct categories; one where the boundary layer was laminar and another where the boundary layer was turbulent. In the laminar category (and consequently low Reynolds number range), a small variation in the Reynolds number caused a large variation in the base pressure. From experimental data, it was determined that large variations in

the base pressure ( $\approx 50\%$ ) could be obtained by simple modifications of the contour on the model nose (with surface roughness having a similar effect). In the turbulent category, there is very little variation in the base pressure with an increase in Reynolds number or a change in the model surface. Thus, Kurzweg determined that the base pressure was not solely dependent on the Mach number, but it was also closely related to the boundary layer characteristics.

Whitmore and Moes [34] performed a base drag reduction experiment during the X-33 linear aerospike SR-71 experiment flight program. For the experiment, a scale X-33 fore-body model was attached to an SR-71. Experiments were performed on smooth and rough surfaces over a Mach number that ranged from high subsonic through transition into low supersonic. Preflight calculations estimated that a base drag reduction of 8-14% was possible with the proposed type of surface roughness. The flight test data showed that the surface roughness was able to reduce the base drag by approximately 15% and that the drag reduction appeared even at supersonic speeds. However, an overall net drag reduction was not achieved because the reduction in base drag was not enough to overcome the increase in viscous fore-body drag and fore-body pressure drag caused by the surface roughness. These results underscore the potential of using viscous fore-body drag as a useful drag reduction tool.

Saltzman *et al.* [23] reviewed subsonic lift and drag characteristics of seven lifting body vehicle configurations with truncated bases. The base pressures were used to calculate base drag and compared with the relationship developed by Hoerner. The important conclusions drawn by the review are as follows. First, the data from the seven lifting body configurations supported the correlations that Hoerner developed for two and three dimensional objects. Secondly, Hoerner's relationships can be recast into total drag versus viscous fore-body drag with total drag minimized at an optimum value of viscous fore-body drag (this concept gives rise to the "drag bucket"). Third, the magnitude of the viscous fore-body drag that defines the bucket is dependent on the ratio of the base area to the wetted area of the vehicle. It was further concluded that a vehicle with a large base-area-to-wetted-area ratio could benefit from surface

roughness at low lifting conditions.

Rowe *et al.* [22] studied the influence of boundary-layer thickness on base pressure and vortex shedding frequency. Two models were studied during the experiment: the first was a subsonic model and the second was a transonic model. Both models were flat plates with elliptical leading edges and square cut trailing edges. The free-stream Reynolds number (based on model chord length) was  $1.7 \times 10^6$  for the subsonic case and  $2.15 \times 10^6$  for the transonic case. Wires were introduced at the end of the leading-edge curvature to change the thickness of the boundary layer before separation. The results of the study showed that, for turbulent flows with zero streamwise pressure gradient, an increase in boundary-layer thickness caused an increase in base pressure and a decrease in the vortex shedding frequency.

A wind tunnel investigation by Whitmore *et al.* [35] studied bluff body drag reduction using fore-body surface roughness. The tests were conducted on a two-dimensional cylinder with a blunt afterbody over Reynolds numbers of  $1.225 \times 10^5$  –  $2.25 \times 10^5$ . The study had two main objectives: to conclusively demonstrate the “drag bucket” concept discussed previously, and to establish a set of conditions that describe the region where an increase in viscous fore-body drag will result in an overall drag reduction. The results of the test showed that the “drag bucket” existed with a peak drag reduction of approximately 15%. The study also concluded that the base drag coefficient that corresponds to the minimum total drag lies in the range 0.225 to 0.275. This value is slightly lower than the range provided by Hoerner’s data (0.25 to 0.30).

The use of viscous fore-body drag to reduce total drag is still in a stage of infancy with several questions left to be answered. For example, what are the effects of Reynolds number and the ratio of base to fore-body wetted area? This study is a follow on to the work of Whitmore *et al.* [35]. In this study however, the Reynolds number will be an order of magnitude higher ( $2.5 \times 10^6$ ), the surface roughness effects are greater, and the model will allow for a variation in the base to fore-body wetted area ratio.



## Chapter 2

# Experimental Setup and Instrumentation

### 2.1 Overview

In order to study the effects of viscous fore-body drag on base drag, a ramp model was constructed and various instrumentation was implemented to measure the quantities needed. The following chapter provides details about the ramp model and the instrumentation used.

### 2.2 Ramp Model

In order to study the effect of viscous fore-body drag on base drag, a two-dimensional ramp model was fabricated that allowed for two ramp angles (3 and 5 degrees). Since the ramp model was designed to fit into an existing flat plate model for the wind tunnel, a flat surface extended from the trailing edge of the ramp. However, it should be noted that the introduction of the symmetry plane will modify the results from that of a full wedge, so a comparison between the two cases will not be made. The ramp was designed to interface at a point tangent to the elliptical leading edge of the flat plate such that a smooth transition occurred. The base area increased with

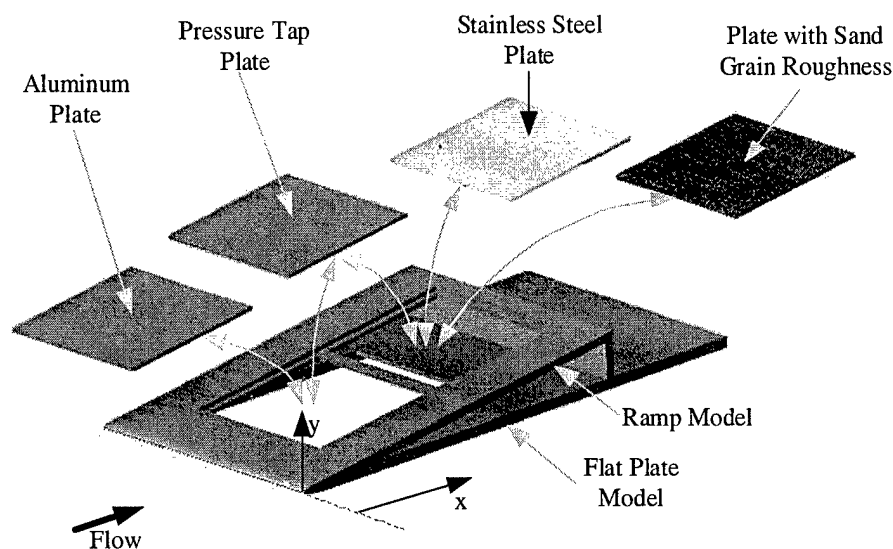


Figure 2.1: Schematic of ramp model with interchangeable plates.

ramp angle since the length of the model was held constant. As shown in Fig. 2.1, the ramp model was designed with locations for two interchangeable plates. The interchangeable plates included a plate with pressure taps for measuring the fore-body pressure gradient, a polished stainless steel plate for use with oil-film interferometry, and plates with three sizes of sand grain roughness used to manipulate the viscous fore-body drag. The base area of the ramp was fitted with pressure taps to measure the base pressure (see Fig. 4.2(b)). In this experiment the term fore body refers to the portion of the model that begins at the tip of the nose and terminates at the separation point.

Surface roughness was used in this experiment to manipulate the viscous fore-body drag. Only a brief discussion of the effects of surface roughness and favorable pressure gradient on turbulent boundary layers is presented here since this study focuses on the effects of viscous fore-body drag on base drag. For a detailed discussion of turbulent boundary layers with surface roughness and favorable pressure gradient effects, see Li *et al.* [16].

Grain Size	Screen Size Large	Screen Size Small	k (mm)
Small	50	70	0.25
Medium	20	25	0.8
Large	7	8	2.2

Table 2.1: Details of sand grains used to produce roughness. Here  $k$  is equivalent to the sand grain diameter  $D_s$ .

Three grain sizes of silicon sand were used to provide different levels of surface roughness for this experiment. Sand of a known grain size distribution was purchased. Further control of the sand grain size was provided by sifting the sand through mesh screens of known size. A summary of the sand grain and mesh sizes is provided in Table 2.1. Once a uniform sand grain size was obtained, the sand was fixed to the surface of the interchangeable plates using a spray-on adhesive. Pictures of the sand grains fixed to the surface of a plate are shown in Fig. 2.2.

The effect of roughness can be partially characterized using  $k^+ \equiv ku_\tau/\nu$ , the equivalent roughness in wall units. Here  $u_\tau$  was obtained from a non-linear fit of the wall-wake law discussed in the Hot-wire Anemometry section. Using  $k^+$ , surface roughness can be categorized into three regimes: hydraulically smooth, transitionally rough, and fully rough. In the hydraulically smooth regime,  $k^+ < 5$ , the roughness resides well within the viscous sublayer and the velocity profile of the boundary layer is equivalent to that of a smooth wall. In the transitionally rough regime,  $5 < k^+ < 70$ , small perturbations in the sand grain size have a large effect on the velocity profile of the boundary layer. In the fully rough regime,  $k^+ > 70$ , the skin friction coefficient becomes independent of  $k^+$ . Fig. 2.3 shows the variation of  $k^+$  with  $Re_x = (U_e x)/\nu$  along the surface of the model for two ramp angles. For the cases studied here, the medium and large sand grains produced fully rough surfaces, whereas the smallest sand grains were transitionally rough.

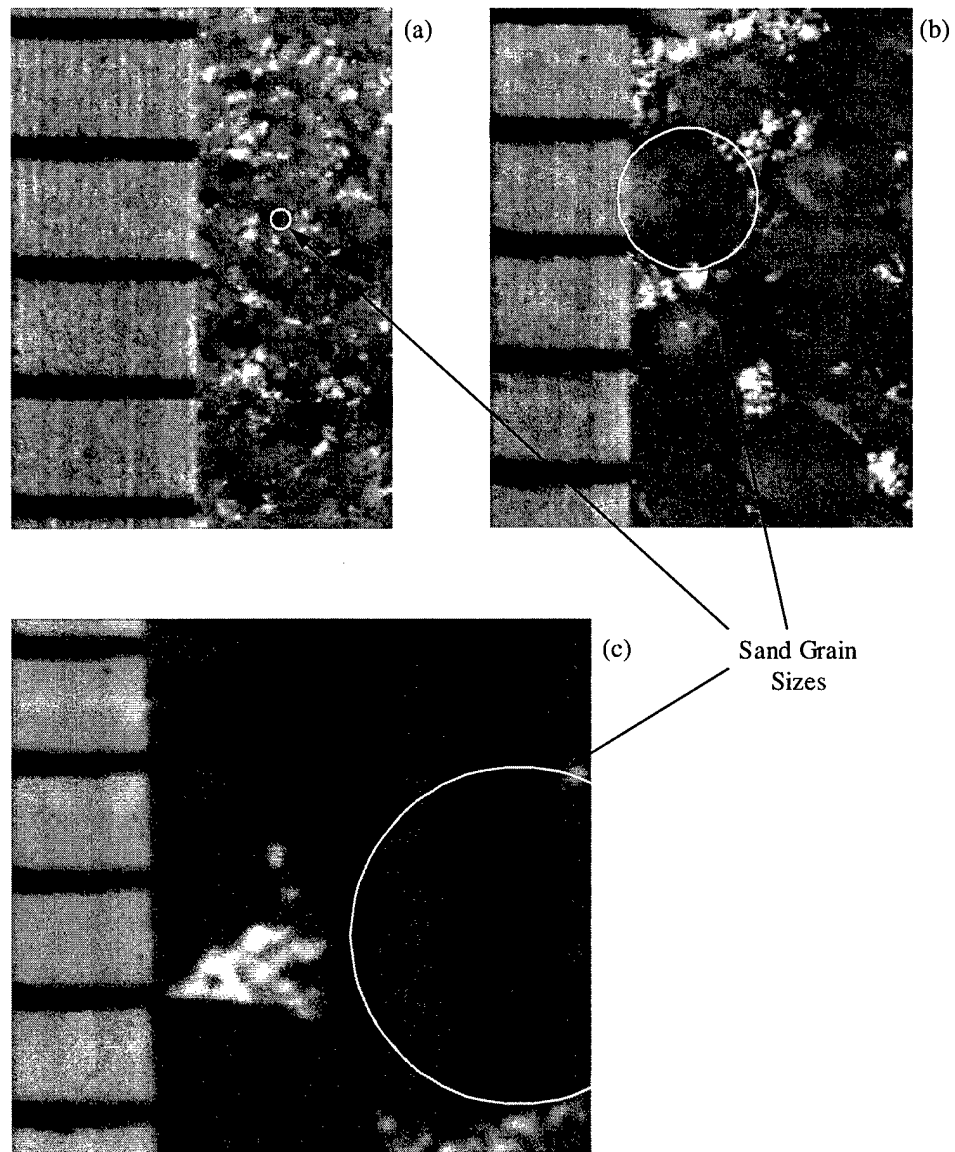


Figure 2.2: Image of sand grains fixed to plate surface: (a) small, (b) medium, and (c) large sand. One ruler division is .794mm.

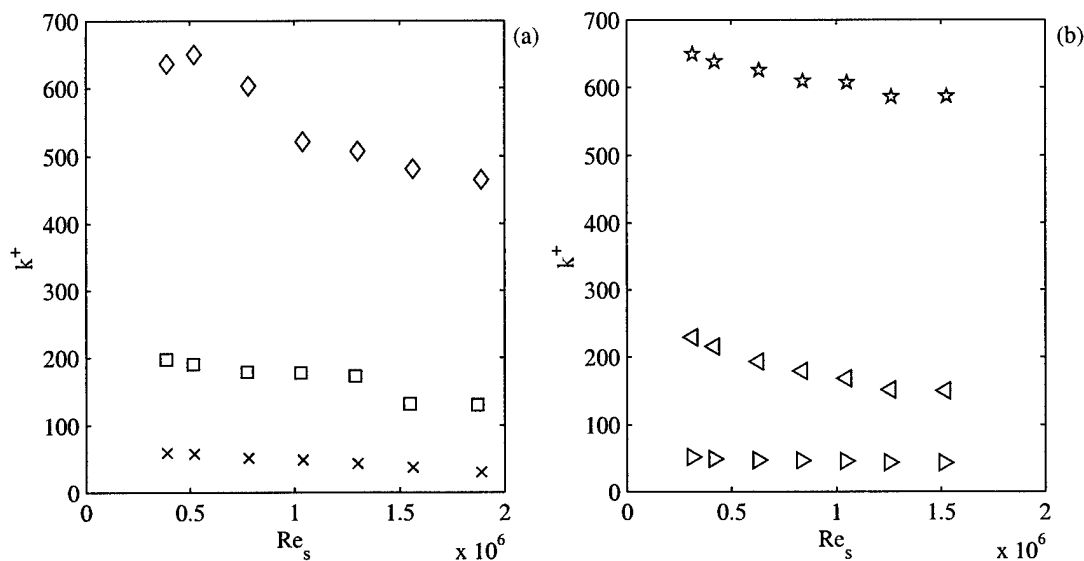


Figure 2.3: Roughness height in wall variables: (a) 3 degree ramp with  $U_\infty = 50$  m/s and (b) 5 degree ramp with  $U_\infty = 40$  m/s. See Table 4.3 for symbol definitions.

## 2.3 Ambient and Reference Conditions

A mercury barometer was used before each experiment to measure the ambient pressure,  $p_{\text{atm}}$ . The ambient temperature was monitored using a thermocouple measured by a 16-channel thermocouple reader (Stanford Research Systems model SR-630). The reference velocity was measured using a Pitot tube mounted through the ceiling or the side wall of the wind tunnel test section. The differential pressure from the Pitot tube was measured using a 100 torr pressure transducer (MKS Instruments).

## 2.4 Oil-film Interferometry

Oil-film interferometry was used to determine the viscous fore-body drag for the smooth cases tested here. A brief description of oil-film interferometry is provided here. For more information on oil-film interferometry see Tanner and Blows [30],

Nominal Viscosity cSt	Density kg/m <sup>3</sup>	Measured Viscosity cSt
10	935	13.0
50	960	56.8
100	964	104.8

Table 2.2: Properties of Dow Corning 200 fluid used for oil-film interferometry measurements.

Tanner [29], Monson and Mateer [18], Zilliac [36], and Naughton and Sheplak [20].

Oil-film interferometry uses oil placed on the surface of a model to determine the local shear stress. As the tunnel runs, the shear stress  $\tau$  causes the oil to thin into a wedge-like shape (see Fig. 4.4). An extended monochromatic light source is used to illuminate the model surface. The light reflects from the air-oil interface as well as the oil-surface interface. The beams reflected from the interfaces are then captured by an imaging device (typically a CCD camera) and form an interference pattern. The interference patterns form because the reflected beams either constructively or destructively interfere with each other (depending upon the oil thickness). The spacing between destructive interference bands is related to the local oil height, which with some additional information can be used to calculate the local skin friction.

### 2.4.1 Oil Calibration

The analysis of oil-film fringes requires accurate knowledge of the viscosity of the oil used. The oils used in this experiment were calibrated using a Canon-Finske constant temperature viscometer. A sample of oil was charged into a glass viscometer tube used with the system. The tube was then inserted into a constant temperature oil bath and allowed to come to an equilibrium temperature (approximately 68 °F). A vacuum was then placed on one side of the tube, causing the oil to flow towards the low pressure. In the process, two bulbs in the tube were filled with oil. The time

required to fill the bulbs was recorded and was used to calculate the actual viscosity.

The oils used in this experiment were silicon oils from Dow Corning. The important properties of these oils including the nominal and measured viscosities are listed in Table 2.2.

### 2.4.2 Image Acquisition System

An “in-line” image acquisition system was developed for oil-film interferometry measurements in this study. A schematic of the assembled oil-film data acquisition system is shown in Fig. 2.4, and a picture of the system is shown in Fig. 2.5. An “in-line” system keeps optical distortions to a minimum and provides maximum access to a model surface. The light that is produced by the source strikes a piece of ground glass to generate an extended uniform light source. Light from the source travels to the beam splitter where approximately 50% of the light is transmitted and continues toward the model surface. Light is reflected from the oil and model surface back toward the beam splitter where approximately 50% of the reflected light is directed toward the digital camera. An optical bandpass filter is used to reject light outside of a narrow wavelength specified (this is required by oil-film interferometry). The light passing through the filter is captured by the digital camera and is stored as an image on a computer. Key components of the oil-film interferometry image acquisition system are shown in Table 2.3.

The constraints of the “in-line” image acquisition system required components (the light source, ground glass, and optical bandpass filter) with certain characteristics discussed below. A mercury grid lamp (see Fig. 2.6) was selected as the light source because the serpentine tube structure provided a good extended source of light. Mercury also has a spectrum that contains several strong peaks, which is desirable because oil-film interferometry requires a single wavelength of light to accurately determine the height of the oil. The 435.8 nm peak in the mercury spectrum was chosen because it provided the strongest and shortest visible wavelength. The strength of light at a given wavelength is important because a high value translates into a decrease in the

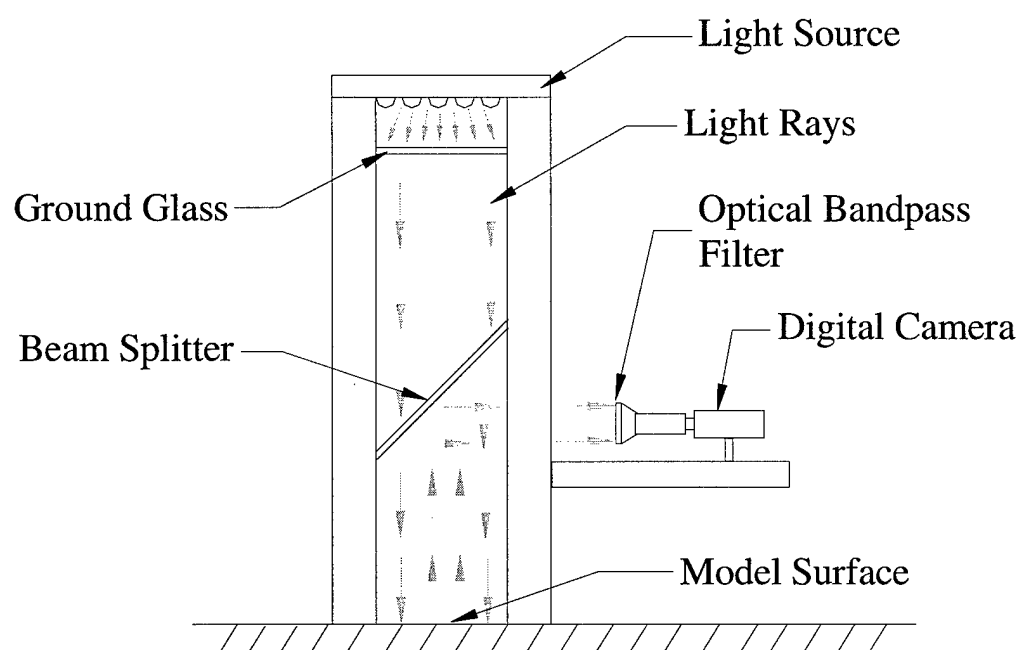


Figure 2.4: Schematic of "in-line" oil-film interferometry image acquisition system.



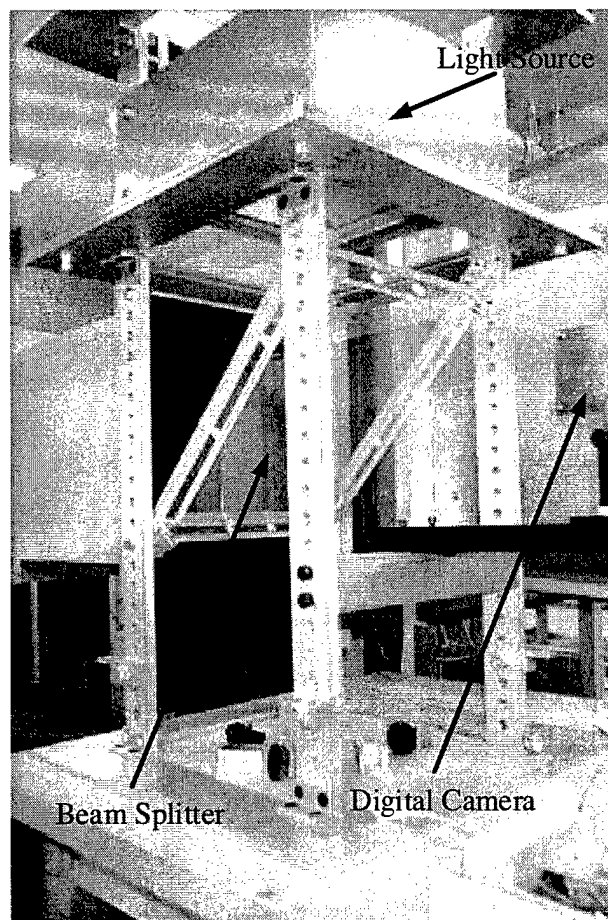


Figure 2.5: "In-line" oil-film interferometry image acquisition system.

Component	Manufacturer/ Part Number	Description
Light Source	BHK/ 88-9660-22	Mercury Grid Lamp, 1000 W, 10in. $\times$ 10in.
Ground Glass	Glass-Tek Industries	Borosilicate Glass, 11in. $\times$ 11in.
Beam Splitter	Edmund Scientific/ H72502	Mirror Type, 254mm $\times$ 356mm, 60/40 transmission/reflection
Optical Bandpass Filter	Ealing/ 35-3334	50.8mm $\times$ 50.8mm, 435.8 nm center wavelength, 7.4 nm bandwidth FWHM
Digital Camera	Pulnix/ TM-9701	8-bit grayscale CCD, Pixel: 768(w) $\times$ 484(h)

Table 2.3: Oil-film interferometry image acquisition system parts list.

sensitivity needed by the imaging device to capture the light. The short wavelength is desirable because it produces a higher fringe density (more fringes per unit length) in the oil-film interferograms. The ground glass was used to diffuse the light and help increase the extended field produced by the mercury lamp. Borosilicate glass was chosen because it has a high temperature handling capability, which is required since the glass is mounted near the lamp. Finally, the optical bandpass filter was chosen to single out one wavelength of light produced by the lamp.

### 2.4.3 Data/Image Acquisition Software

Interferograms were acquired using a digital CCD camera (Pulnix model TM-9701) and a digital frame grabber (National Instruments model IC-PCI with an AM-DIG image acquisition module) controlled by LabView software. The image acquired by the frame grabber was stored on a computer for later analysis. The transfer of the data from the camera to the computer was completely digital so there was no decrease in image quality. As an image was acquired from the camera, the temperatures from four thermocouples embedded in the stainless steel plate were also measured. The

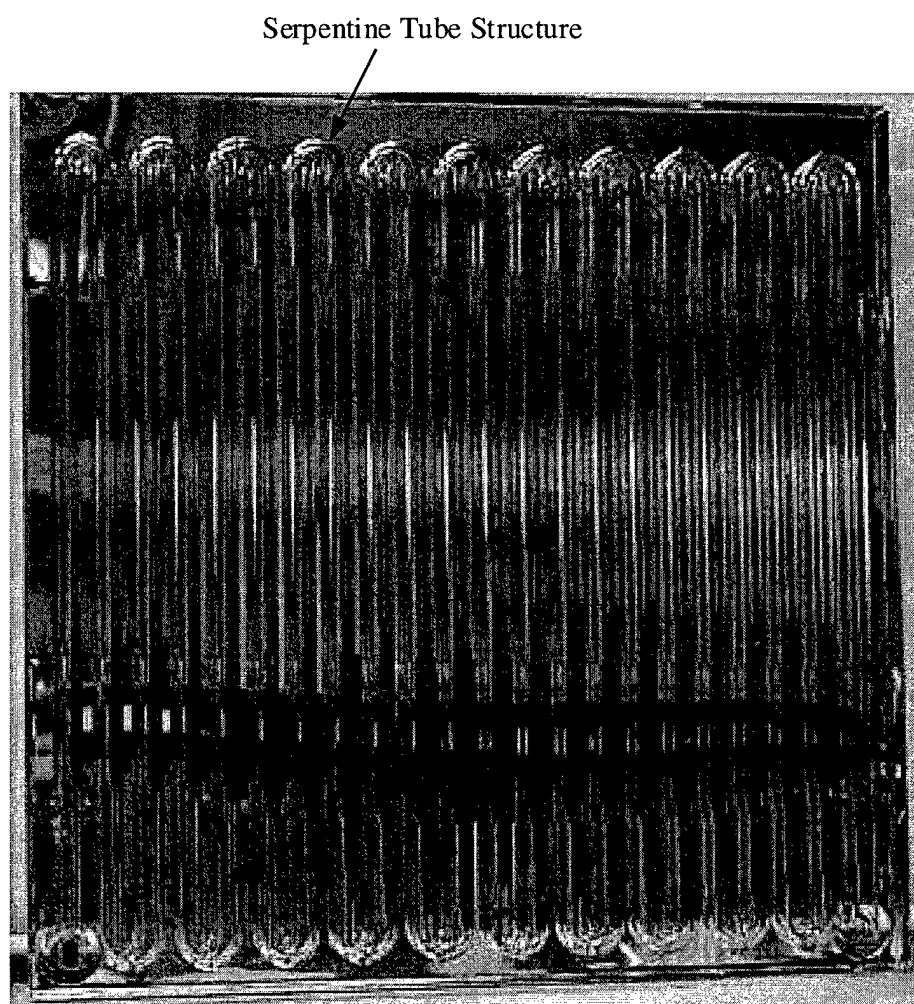


Figure 2.6: Mercury grid light source used with oil-film interferometry image acquisition system.

temperatures were used during analysis to compensate for changes in the oil viscosity. The free-stream pressure was monitored for the duration of the wind tunnel run.

#### 2.4.4 Interferogram Analysis

The method used to analyze the oil film interferograms used in this study will be described in some detail since it is a combination of several techniques that have been used in the past. A three-step process was used to analyze the images here: the oil-film image was registered, the fringe patterns were identified, and each fringe pattern was analyzed. Each of these steps is described below.

Before the interferogram can be processed, it must be registered so that the pixel locations in the image can be related to their actual location in space. Registration marks are applied to the model (the crosses visible in Fig. 2.7) to make image registration possible. On models with curvature, surfaces viewed from an angle, or images with significant distortion, registration methods such as those outlined by Cattafesta and Moore [4] should be used. However, since the interferograms obtained here are taken at normal incidence on a flat surface, a simpler technique is used. A global transformation (the 'affine' transformation, see reference [2], is applied to the image to map pixel space into known physical space).

Identification of the fringe patterns to be analyzed is the next step in the analysis procedure. Since there are only approximately ten fringe patterns per image, each fringe pattern is selected interactively. A point upstream of the oil leading edge is selected, and the length and direction of the line to be analyzed is specified. An interference pattern and the line selected for analysis are shown in Fig. 2.7.

The analysis of the identified fringe patterns is the last step. First, the intensity along the line shown in Fig. 2.7 is extracted from the image. The variation of intensity along this line is shown in Fig. 2.8(a). To determine the shear stress, the peaks and valleys of this line are isolated. Elements of the fringe detection method discussed by Decker *et al.* [8] and Decker and Naughton [7] are used for this purpose. The Fourier transform of the extracted line is taken and the non-zero frequency with maximum

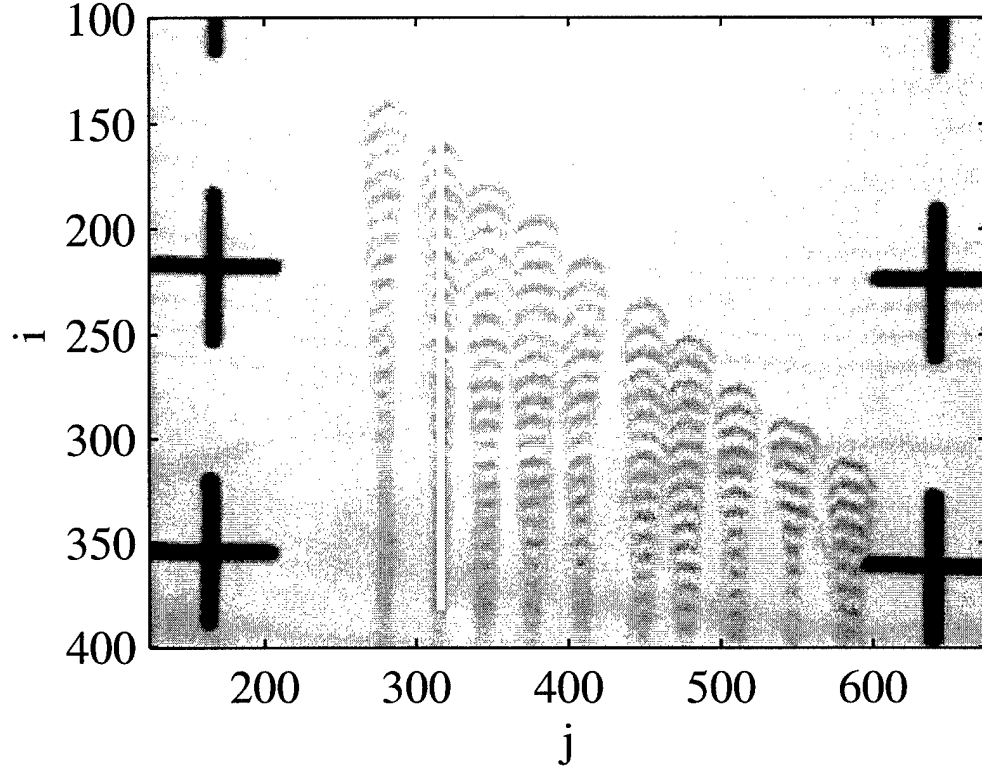


Figure 2.7: Interferogram with analysis line overlaid. Note the crosses in the figure that are used for registration purposes.

amplitude is determined as shown in Fig. 2.9. Using this maximum frequency, an interrogation signal is constructed using a single-period cosine as shown in Fig. 2.8(b). Next, the cross-correlation  $R_{i,if}$  of the original signal and the interrogation signal is determined from which the cross-correlation coefficient  $\rho_{i,if}$  is determined:

$$\rho_{i,if} = \frac{R_{i,if}}{\sqrt{R_{i,i}(0)R_{if,if}(0)}}, \quad (2.1)$$

where  $R_{i,i}(0)$  and  $R_{if,if}(0)$  represent the value of the auto-correlations at an offset of zero. The resulting cross-correlation coefficient is shown in Fig. 2.8(c). In this figure, it is evident that the peaks of  $\rho_{i,if}$  correspond to intensity minima in the original signal, whereas the minima of  $\rho_{i,if}$  correspond to intensity maxima. It should also

be noted that the cross-correlation coefficient signal is somewhat cleaner than the original signal and the peaks and valleys of  $\rho_{i,if}$  lie on opposite sides of zero.

To determine the shear stress, the height of the oil at the intensity maxima and minima is needed. First, the locations of the maxima and minima that exceed a user-specified threshold of  $\rho_{i,if}$  are determined. For the intensity distribution in Fig. 2.8(a), the peaks with  $\rho_{i,if} > 0.05$  are shown as symbols in Fig. 2.8(c). It can be shown that these peaks and valleys correspond to specific oil thicknesses given by

$$h = \frac{k\lambda}{4\pi} \frac{1}{\sqrt{(n_{oil}^2 - n_{air}^2 \sin^2(\theta_i))}}, \quad (2.2)$$

where  $k$  is the fringe number (the first valley is 1, the first peak is 2, *etc.*),  $\lambda$  is the illumination wavelength,  $\theta_i$  is the incident light angle, and  $n_{oil}$  and  $n_{air}$  are the oil and air indices of refraction. Due to the difficulties of determining the peak/valley locations with subpixel accuracy, the height data shown in Fig. 2.8(d) is fit using a second-order curve fit, and the result is shown in Fig. 2.8(d). A second-order curve fit is used since it permits a varying shear stress that a first-order fit would eliminate (a linear height increase corresponds to constant shear stress).

Once the oil-film height is known, the shear stress is determined using a modification of the method given by Garrison and Ackman [10]. Their approach uses the streamline form of the oil-film equation first given by Tanner and Blows [30], which can be used to solve iteratively for the shear stress (see reference [10] for details):

$$(\tau_{i+1})^{1/2} = \frac{\int_0^x \left[ \frac{n}{\tau_i} \right]^{\frac{1}{2}} dx}{h \sqrt{(n)} \int_0^t \frac{dt}{\mu}}, \quad (2.3)$$

where  $h$  is the oil-film height,  $n$  is the streamline divergence,  $\mu$  is the oil viscosity,  $t$  is time,  $x$  is the distance measured along the streamline,  $\tau_{i+1}$  is the updated value of the shear stress and  $\tau_i$  is the previous value. Fig. 2.10 shows the coordinate system used for the streamline form of the equation. Eq. 2.3 can be modified by dividing by

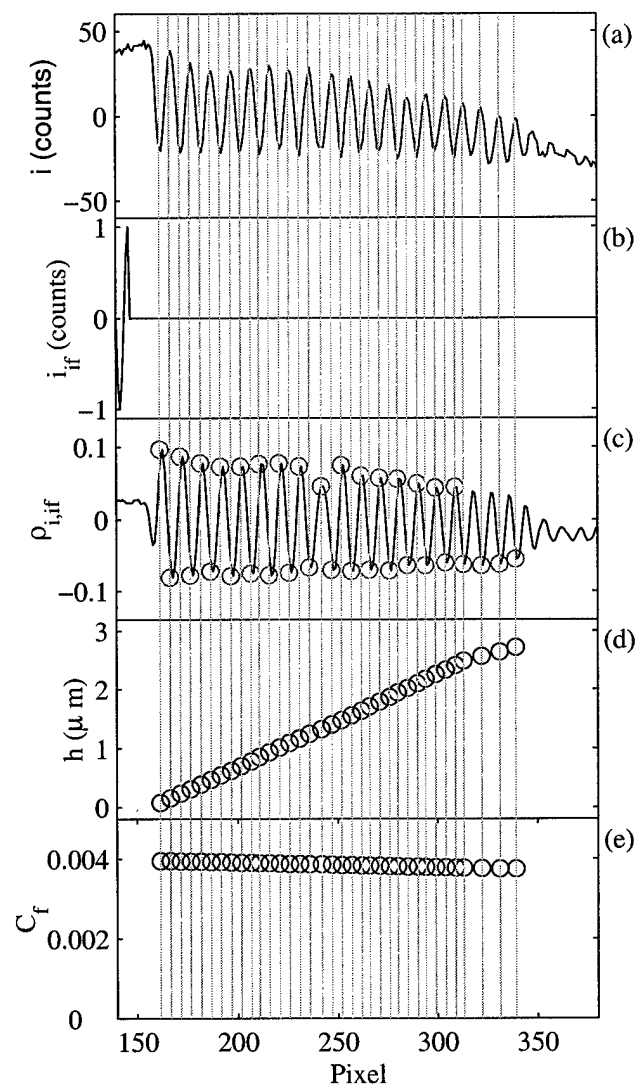


Figure 2.8: Steps of fringe analysis to determine skin friction coefficient: (a) Intensity along the line shown in Fig. 2.7; (b) Interrogation fringe; (c) cross-correlation coefficient; (d) oil-film height; and (e) skin friction coefficient.

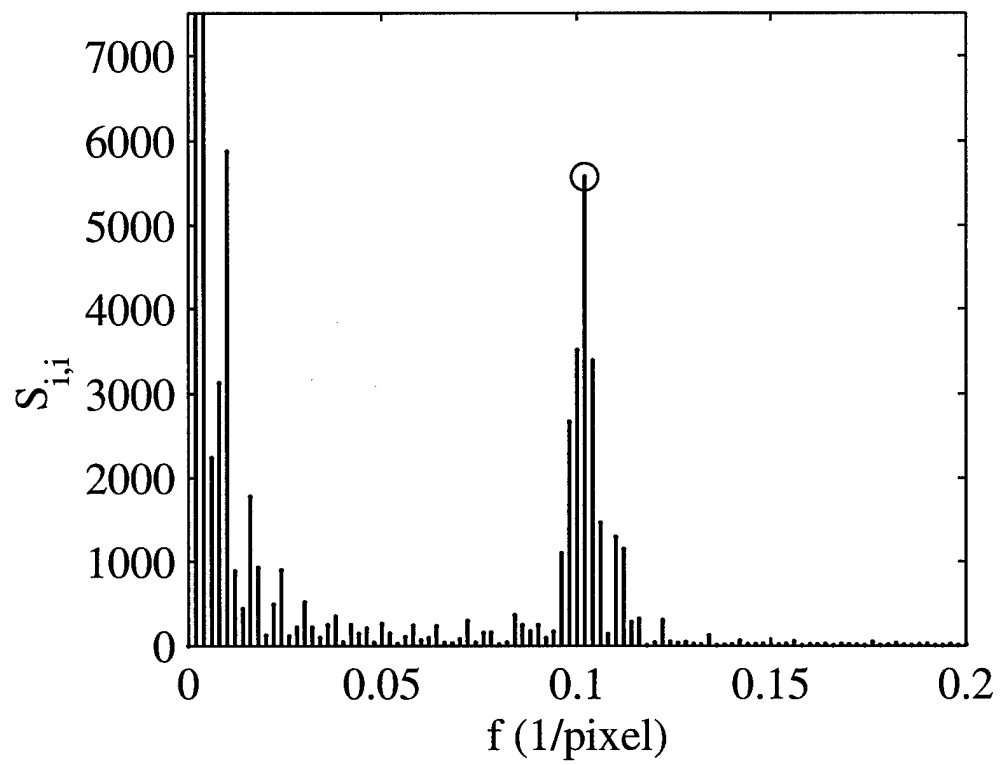


Figure 2.9: Auto-spectral density of the intensity signal in Fig. 2.8(a). Note the peak located away from zero frequency.



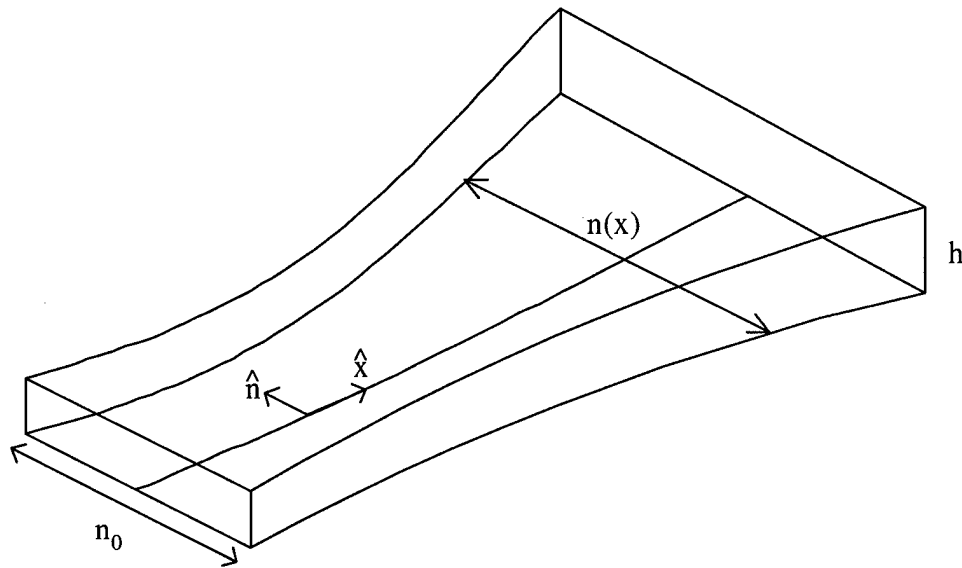


Figure 2.10: Streamline-based coordinate system used for oil-film interferogram analysis.

the dynamic pressure  $q$  to produce

$$(C_{f,i+1})^{1/2} = \frac{\int_0^x \left[ \frac{n}{C_{f,i}} \right]^{\frac{1}{2}} dx}{h \sqrt{(n)} \int_0^t \frac{q}{\mu} dt}, \quad (2.4)$$

where  $C_f$  is the skin-friction coefficient, and  $q$  is the dynamic pressure of the air flow. To use Eq. 2.4, an initial guess for the skin friction is required. As suggested by Garrison and Ackman [10], an approximate estimate for  $C_f$  can be obtained by assuming the shear stress is constant

$$C_{f,1} = \frac{\mu x}{q h t}. \quad (2.5)$$

The converged  $C_f$  distribution for the intensity distribution shown in Fig. 2.8(a) is shown in Fig. 2.8(e).

The purpose of using the approach outlined here was to provide a large amount of data that could be spatially averaged to produce a distribution with a low random

error. As a result, the shear stress distributions shown later in this paper represent averages of many data points.

## 2.5 Hot-Wire Anemometry

Instantaneous velocities in the boundary layer were measured using a single wire, constant temperature hot-wire anemometry system. The measurements were made with a  $2.5 \mu\text{m}$  boundary layer hot-wire probe (Auspex Corp.) with typical resistances of  $4\Omega$ . The probe was connected to an A.A. Labs An-1003 anemometer. The output of the anemometer was split into two signals and sent to a dual-channel low pass filter (Stanford Research Systems model SR-640). The mean voltage was determined by low-pass filtering one signal at 10 Hz. The fluctuating voltage was determined by AC coupling the second signal to the second channel of the low-pass filter and filtering at 90% of the Nyquist frequency. Both filtered signals were acquired using a National Instruments A/D board controlled by LabView software. Once acquired, the voltages were converted to velocities using Kings' law with the constants determined in a calibration process before the run.

The boundary layer profiles were obtained using a computer controlled traversing system. A typical survey contained 50 y-locations, with the system acquiring 256k points at each location at a sampling rate of 10 kHz.

In order to estimate the viscous fore-body drag from the rough surface measurements, the logarithmic law-of-the-wall and the law-of-the-wake were combined to form the wall-wake law for rough surfaces (from Clauser as reported in [12]),

$$u^+ = \frac{1}{\kappa} \ln(y^+) + B + \frac{2\Pi}{\kappa} W\left(\frac{y}{\delta}\right) + \Delta U^+, \quad (2.6)$$

where

$$W\left(\frac{y}{\delta}\right) \approx \sin^2\left(\frac{\pi y}{2\delta}\right). \quad (2.7)$$

Here  $u^+ \equiv u/u_\tau$  is the velocity in wall units,  $u_\tau$  is the friction velocity,  $\delta$  is the boundary layer thickness,  $\kappa$  and  $B$  are von Karman's constants (0.41 and 5.2),  $y^+ \equiv$

$(yu_\tau)/\nu$  is the distance from the wall in wall units,  $\Pi$  is Coles' wake parameter and accounts for pressure gradient effects, and  $\Delta U^+$  is introduced to account for the shift of the curve due to surface roughness effects (from reference [12]). A non-linear least-squares Gauss-Newton curve fit ([14],[17]) was applied to Eq. 2.6 using the  $u$  and  $y$  data from the hot-wire surveys. This non-linear curve fit provides values for five parameters:  $y_{\text{offset}}$ ,  $u_\tau$ ,  $\Pi$ ,  $\delta$ , and  $\Delta U^+$  (for the rough surface cases). It should be noted that  $y_{\text{offset}}$  is a value used to shift  $y$  since the location of the surface is not easily determined on rough surfaces. The wall shear stress (and eventually the viscous fore-body drag) was determined from the curve fit since  $\tau_w = \rho u_\tau^2$ . For additional details of the hot-wire system, data analysis, and uncertainty, see Li [15].

## 2.6 Pressure Measurement

Two different types of pressure measurement were made in this experiment: measurements of the base pressure along with measurements of the fore-body pressure. Each of these measurements required a different data acquisition that is described below.

Base pressures were measured from pressure taps embedded in the base of the model (see Fig. 4.2(b)) using two Pressure Systems Inc. model 9010 pressure transducers. Each model 9010 transducer has 16 channels, with a full scale range of 0-10 in. of water and provides temperature compensation. The transducer output was read by a computer (using LabView software) via an RS-422/RS-232 connection. In order to build up useful statistics for the base pressure in a given run, 1000 data points were taken on each of the 32 channels with an average sampling rate of 0.25 Hz.

The fore-body pressure gradient was measured using an MKS Instruments pressure transducer. The transducer has one channel with a full scale range of 0-100 torr. In order to read the 24 pressure taps necessary to determine the pressure gradient, a Scanivalve switching system was utilized. The Scanivalve allowed a single channel pressure transducer to sequentially measure pressures from a number of pressure

taps. The output of the pressure transducer was read by a National Instruments A/D board using LabView software. For each pressure tap 1000 points were acquired at a sampling rate of 100 Hz.

## 2.7 Test Cases

In order to assess the effect of viscous fore-body drag on base drag, several test cases were run. Table 4.3 summarizes the test cases used in this study. Three different parameters were varied in this test. Four levels of surface roughness were used to vary the fore-body viscous drag. To change the Reynolds number, the reference velocity was varied. Finally, to modify the base height, the ramp angle was changed. Base and fore-body pressures were measured for each case. To measure  $C_f$ , oil-film interferometry was used for the smooth surface cases and hot-wire anemometry was used for both the smooth and rough surface cases.

## Chapter 3

# Automated Interference Fringe Pattern Recognition

### 3.1 Introduction

Interferometry has been used as a powerful tool in many applications including such diverse areas as optical component inspection and density mapping in aerodynamic flows. Although interferometry is powerful, the technique poses some challenges when the interferograms are processed. Some examples of the challenges that have been overcome are phase unwrapping and fringe counting.

One measurement technique, thin-oil-film interferometry, uses interferometry to determine surface shear stress in aerodynamic flows. In this technique, oil is applied at multiple locations on the surface of a wind-tunnel model (henceforth referred to as the model). When subjected to an air stream, the shear stress that develops on the model surface induces flow in the oil thus creating a thin film (thickness is on the order of microns). Illuminating these thin films with quasi-monochromatic light produces interference patterns. If an image of the interference pattern is captured some time after the air flow has started, the spacing between interference fringes can be related to the shear stress acting on the oil film. Typically, hundreds of oil drops or lines are applied to the model surface so that the surface shear stress may be determined at

many locations simultaneously.

Currently, the locations of the interference patterns that form on the model surface are selected by the user, a time-consuming and tedious process. The methods presented here have been developed to automate the fringe-detection process to speed the analysis and to reduce user interaction. The results of applying the fringe-detection method to typical interferograms indicate that a large percentage of fringe-containing regions may be detected. Although this fringe-detection method has been developed specifically for oil-film interferometry, similar methods may be used for other interference fringe recognition purposes.

### 3.2 Oil Film Interferometry for Skin Friction Measurement

In order to provide the context within which the present fringe-detection methods have been developed, a brief overview of oil-film interferometry is provided. For a more complete description of the method, see the review by Naughton and Sheplak [20].

When an oil is applied to a model, shear stress caused by the flow of air over the model causes the oil to thin (see Fig. 3.1). Squire [27] first recognized the relationship between the shear stress and the height of an oil film, but Tanner & Blows [30] were the first to apply oil films to measure shear stress. In general, the motion of the oil film is dependent on the forces acting on it including forces due to aerodynamic shear stress  $\tau$ , aerodynamics pressure  $P$ , gravity  $g$ , and surface tension. In many cases, the shear stress forces dominate, and the equation governing the height of the oil  $h$  is given by

$$\frac{\partial h}{\partial t} + \frac{\partial}{\partial x} \left( \frac{\tau_x h^2}{2\mu} \right) + \frac{\partial}{\partial z} \left( \frac{\tau_z h^2}{2\mu} \right) = 0. \quad (3.1)$$

Here,  $x$  and  $z$  are the spatial variables in the plane of the surface,  $t$  is time,  $\tau_x$  and  $\tau_z$  are the components of the shear stress on the surface, and  $\mu$  is the dynamic viscosity.

When the surface shear stress  $\tau$  is constant and acts in the  $x$  direction only and

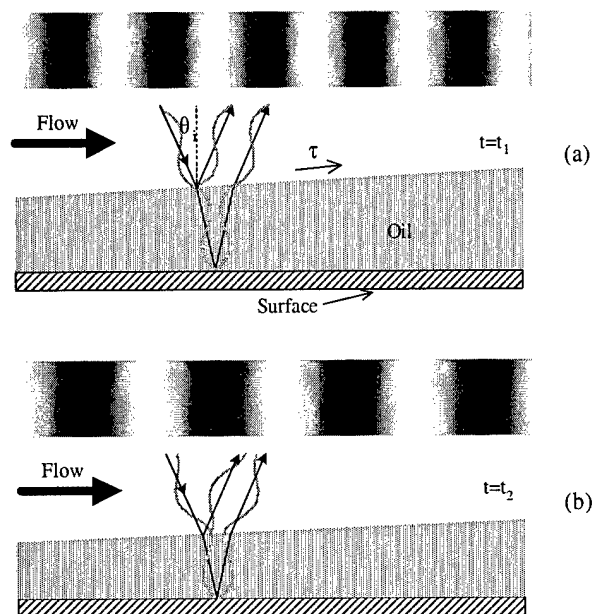


Figure 3.1: Interference fringes produced by Fizeau Interferometry: (a) constructive interference produces bright bands, whereas (b) destructive interference produces dark bands. The interference fringes move as the oil height changes due to the aerodynamic shear stress  $\tau$  acting on the oil film. This figure is used with permission from reference [20].

the oil viscosity  $\mu$  is constant, Eq. (3.1) may be solved to determine  $\tau$ :

$$\tau = \frac{\mu x}{ht}. \quad (3.2)$$

This relationship is independent of the initial oil thickness after a short initial period. Thus, if the height of the oil can be measured, the shear stress may be determined.

To determine the height of thin oil films, Tanner & Blows suggested the use of interferometry. As shown in Fig. 3.1, light illuminating the model reflects from both the air/oil and oil/surface interfaces. If the illumination source is monochromatic and the reflected beams are focused by a lens, the phase difference  $\phi_t$  between the beams produces interference fringes. An example interferogram is shown in Fig. 3.2 in which oil drops applied to a model have thinned when subjected to an air flow. As shown

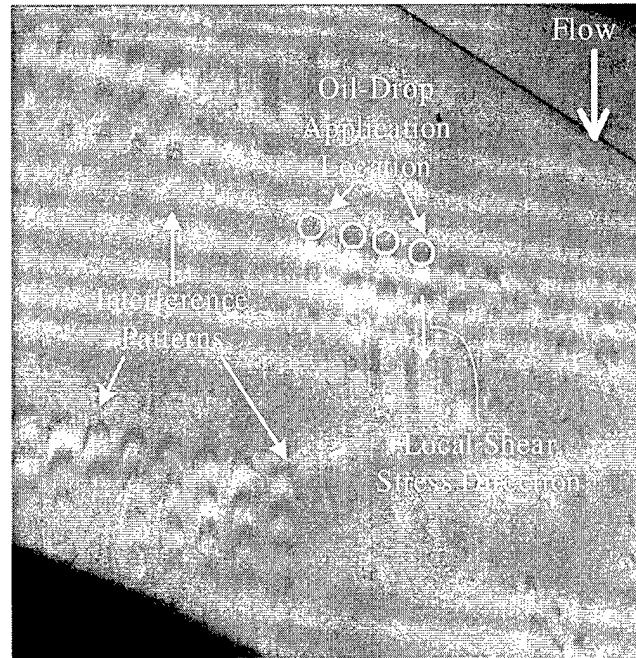


Figure 3.2: Interferogram resulting from oil drops placed at various location on a wing surface. This image is courtesy of David Driver, NASA-Ames Research Center.

in Fig. 3.1, maxima in the intensity pattern occur when the optical paths of the two reflected beams differs by  $i\lambda$ , where  $i$  is an integer and  $\lambda$  is the illumination wavelength. In contrast, minima occur when this pathlength difference is  $(i+1/2)\lambda$ . Many techniques [36, 18] identify the maxima and minima of the fringes where the relative phase difference  $\phi$  is known. An alternative method determines the relative phase distribution using the original intensity distribution and its Hilbert transform [19]. Standard phase unwrapping techniques (e.g. reference [28]) are used to determine the total phase  $\phi_t$  from the relative phase  $\phi$ .

The height of the oil is related to the total phase difference by

$$h = \frac{\lambda\phi_t}{4\pi} \frac{1}{\sqrt{n_f^2 - n_a^2 \sin^2(\theta_i)}}, \quad (3.3)$$

where  $\lambda$  is the illumination wavelength,  $n_f$  and  $n_a$  are the oil and air indices of



refraction, and  $\theta_i$  is the incidence angle. Once the oil height is known, one of several analysis methods [18, 36, 19, 10] may be used to determine the shear stress.

A primary difficulty with the existing analysis methods is that there are often many individual fringe patterns in a single image. As shown in Fig. 3.2, these fringe patterns can cover a significant portion of an aerodynamic model. It is a tedious process to locate all these fringes so that the analysis can proceed.

This paper discusses the results of a recent study that attempts to locate these fringe patterns automatically. The automated fringe detection will reduce the time to analyze oil-film interferograms and, thereby, will encourage the use of the technique.

### 3.3 Theoretical Background

A brief description of the signal processing methods considered for use in fringe detection is presented below. A detailed discussion of the individual techniques and their limitations is presented in reference [8].

Image analysis, artifact reduction and pattern recognition have received considerable attention in the past two decades. Some of the more common techniques among these signal processing methods are the Windowed Fourier Transform (WFT), wavelet analysis, and correlation methods. Use of the windowed Fourier transform to determine a fringe pattern requires specific knowledge of the spectral characteristics of that fringe pattern. Where the spectral composition of the noise significantly overlaps that of the signal and the signal-to-noise ratio is low, this method does not yield optimal results. When the signal-to-noise ratio is sufficiently large, the frequency content of the desired signal may be determined, but its location within the windowed data is unknown. Cut-offs introduced through these methods lead to other considerations such as ringing artifacts (Gibbs phenomena) and ghosting (aliasing). Due to these factors, the windowed Fourier transform, when used alone, is unable to pinpoint locations of the fringe pattern.

Wavelet analysis provides a reconstruction mechanism optimally suited for a self-similar image, where the same phenomenon is repeated at various scales. The image is decomposed into a superposition of dilates and translates of a given pattern, and thus extraneous information is rejected. In the present case, the interference patterns to be detected are known functions. However, the creation of a wavelet similar to these waveforms is difficult, and using wavelets places unnecessary constraints on the function used for the wavelet.

Another approach considered is a correlation method. In this approach, a function representing the interference fringe is correlated with the interferogram. The locations of large positive and large negative correlations identify the locations of the fringe patterns. Correlation methods may be described as FIR filtering, and, indeed, they have an interpretation in terms of both the windowed Fourier transform and the wavelet transform. This approach works well when the spectral content of the interference fringes in the interferogram is known *a priori*. If the spectral content of the interference patterns is unknown, a combination of this method and optimization in frequency space may be employed.

The inability of correlation methods to identify the spectral content of the fringe pattern is overcome by combining the correlation approach with the windowed Fourier transform. In this combined approach, the windowed Fourier transform is used to identify the spectral content of an interference fringe pattern (if one exists) in the image. This spectral content is then used to generate an interrogation fringe that is correlated with the original window in the interferogram.

### 3.4 Fringe-Detection Method

As indicated in Fig. 3.2 and confirmed by theory, the interference fringes are well represented by sinusoidal functions. Therefore, the first interrogation pattern investigated is a single period cosine wave. In this section, a one dimensional model of the correlation algorithm and the corresponding FIR filter for a cosine wave will be

described.

### 3.4.1 Filters Based on Dominant Principal Component Waveforms

Let  $\{I(i) : i = 1, \dots, N\}$  be a digitized signal representing the intensity of the interference pattern in the interferogram image. This signal may be represented as a superposition of sinusoidal waveforms with one principal component at wavenumber  $K$ ,

$$I(i) = A_K \cos\left(\frac{2\pi Ki}{N}\right) + \sum_{k=0}^M a_k \cos\left(\frac{2\pi ki}{N}\right), \quad (3.4)$$

where  $k$  is the wavenumber,  $a_k$  and  $A_K$  are coefficients with  $|a_k| \ll |A_K|$ , and  $0 \leq 2M < N$ . In Eq. (3.4), the correlation method searches for the location of these principal components by constructing

$$R_{I,IF}(i) = \sum_{p=1}^q \overbrace{\cos\left(\frac{2\pi Kp}{N}\right)}^{I_{IF}} I(i-p), \quad (3.5)$$

where  $R_{I,IF}$  is the correlation between the original signal  $I$  and the principal component (or interrogation fringe)  $I_{IF}$ , and  $2q \leq N$ . Clearly  $R(i)$  is large where the principal component signal is large and small where the principal component is absent. Taking the Fourier transform of a windowed region of the original interferogram, identifying the spectral content of the signal desired, filtering the spectral information to isolate the desired signal, and inverse Fourier transforming, yields the filtered signal  $\tilde{I}$ . Finally, the peaks and valleys of the correlation of the interrogation fringe with the windowed region of the original interferogram identify the location of the fringe pattern.

In general, this method may be realized more robustly by designing an appropriate nonrecursive finite impulse response (FIR) filter. A FIR filter is a filter that uses a specific waveform, frequently prescribed by some desired spectral properties, to analyze signals directly in time or space coordinates. A sequence of weights is

constructed  $\{w(m) : m = 1, \dots, N\}$  that incorporates specific frequency response such as bandpass, lowpass, highpass, or a pre-specified frequency filtering with a proper roll-off such as to minimize cut-off errors, and then the filtered signal  $\tilde{I}$  is simply constructed using

$$\tilde{I}(i) = \sum_{m=1}^N w(m)I(i-m). \quad (3.6)$$

If no filtering is performed, then  $w(m)$  is simply the principal component signal, and  $\tilde{I}(i)$  is the desired signal. The idea here is to build the filter directly into the choice of the coefficients  $w(m)$ . That this is possible follows from the commutativity of filtering unwanted signals and detection of the desired signal. Using the expression in Eq. (3.4),  $w(m)$  is obtained by taking the Fourier transform of  $\cos(\frac{2\pi Ki}{N})$ , band-limiting the spectrum using a smooth roll-off, and then inverse Fourier transforming. As will be seen later, the filter is applied to the principal component in the frequency domain prior to inverse Fourier transforming.

The analysis above suggests the creation of precise images from simulation studies of the physical problem and the use of these simulation results for precise rejection of irrelevant data. Although the investigation of this concept has begun, it is not discussed further here.

### 3.4.2 Cosine Interrogation Fringe

To demonstrate the fringe-detection process described above, a cosine interrogation fringe is assumed to be the principal component and is applied to a one-dimensional intensity signal  $I(i)$  extracted from an actual interferogram. Although the cosine interrogation fringe is simplistic, it is effective for locating the peaks and valleys in the interference patterns.

The fringe-detection process using a combined windowed Fourier transform and correlation approach is applied to the slice indicated by the white line through the image shown in Fig. 3.3(a). The vertical lines in the intensity plot and the corresponding black line in the image indicate the window that will be analyzed. The

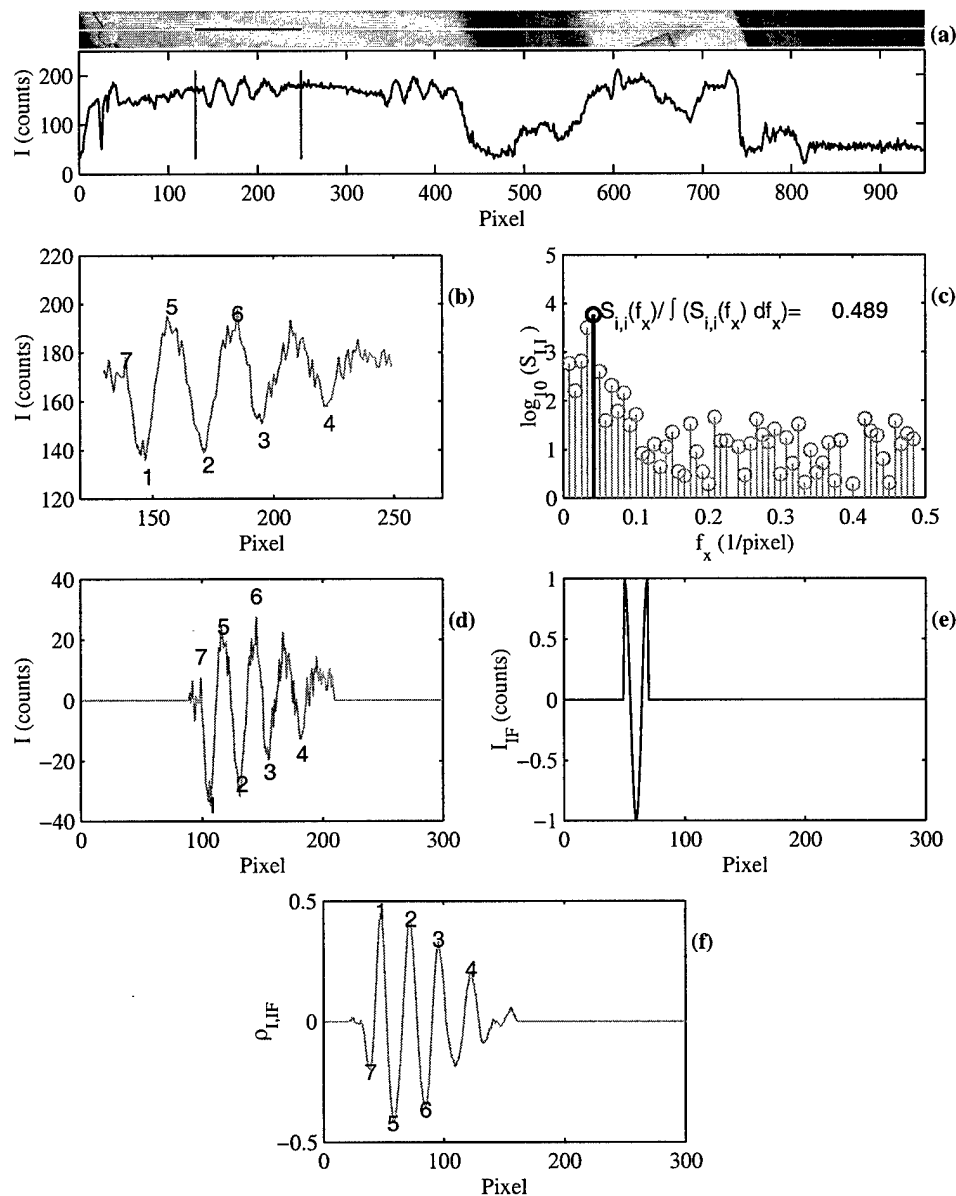


Figure 3.3: One-dimensional example of fringe detection: (a) portion of original image indicating windowed area; (b) intensity distribution within window; (c) autospectral density of intensity distribution; (d) zero-mean, padded intensity distribution; (e) interrogation fringe constructed from peak frequency in autospectral density; (f) cross-correlation coefficient with peaks and valleys identified. Note that the numbers in (f) correspond to the peaks and valleys of the correlation coefficient, which correspond to the peaks and valleys in the interference pattern indicated in (b) and (d).

intensity in the window that is re-plotted in Fig. 3.3(b) clearly shows the presence of a fringe. To identify the frequency of the interrogation fringe that most closely corresponds to the signal in Fig. 3.3(b), the auto-spectral density of the intensity signal  $S_{I,I}$  is determined:

$$S_{I,I} = \frac{1}{N\Delta x} [(\mathcal{F}(I))(\mathcal{F}(I))^*], \quad (3.7)$$

where  $\mathcal{F}(I)$  is the discrete Fourier transform of  $I$ ,  $\Delta x$  is the spatial separation (in pixels here),  $N$  is the number of discrete points in  $I$ , and  $\mathcal{F}(I)^*$  represents the complex conjugate of  $\mathcal{F}(I)$ . The logarithm of the resulting auto-spectral density  $S_{I,I}$  is shown in Fig. 3.3(c). It is evident in the figure that there is a peak in  $S_{I,I}$  (shown in bold) at a non-zero frequency that contains a significant amount of the energy of the entire signal. The frequency at which this occurs is the frequency at which the cosine interrogation fringe is generated. Next, the mean value of the windowed intensity signal is removed, and the resulting signal is padded as shown in Fig. 3.3(d). This signal is then correlated with the cosine interrogation fringe  $I_{IF}$  shown in Fig. 3.3(e). The correlation is computed in frequency space by first determining the cross-spectral density function

$$S_{I,IF} = \frac{1}{N\Delta x} [(\mathcal{F}(I))(\mathcal{F}(I_{IF}))^*], \quad (3.8)$$

and using  $S_{I,IF}$  to determine the cross correlation  $R_{I,IF}$ ,

$$R_{I,IF} = \mathcal{F}^{-1}(S_{I,IF}), \quad (3.9)$$

where  $\mathcal{F}^{-1}$  represents the inverse discrete Fourier transform. To normalize the result, the cross-correlation coefficient  $\rho_{I,IF}$  is determined

$$\rho_{I,IF} = \frac{R_{I,IF}}{\sqrt{R_{I,I}(0)}\sqrt{R_{IF,IF}(0)}}, \quad (3.10)$$

where  $R_{I,I}(0)$  and  $R_{IF,IF}(0)$  represent the values of the autocorrelations at an offset of zero (see reference [3]). The results of the correlation process are shown in Fig. 3.3(f) where it is evident that much of the noise in the original signal is no longer present. To complete the analysis, the peaks and valleys of the correlation coefficient are

determined and are used to locate the peaks and valleys of the original fringe pattern. The numbering of the fringes in Fig. 3.3(f) is ordered from maximum  $\rho_{I,IF}$  value to the smallest  $\rho_{I,IF}$  value still considered to be a peak followed by the most negative  $\rho_{I,IF}$  value to the smallest negative value considered to be a valley. The interference fringe peaks and valleys to which these maxima and minima in  $\rho_{I,IF}$  correspond are identified in Figs. 3.3(b) and (d).

Several comments on the fringe-detection process are needed. First, if there is no fringe evident in the window, there is no peak in the spectrum. By requiring the frequency with the highest autospectral density to contain a significant portion of the energy in the signal, fringe containing windows can be readily identified. Thus, the windowed Fourier transform serves to identify if a fringe is present, and, if so, what frequency the interrogation fringe should be. Second, for those windows containing a fringe, the cross-correlation coefficient  $\rho_{I,IF}$  represents a filtered version of the original signal as can be seen by comparing Fig. 3.3(d) and (f). Seto and Hornung [25, 26] used this property of the correlation to determine the peaks and valleys of interference fringes. In this case, peaks in  $\rho_{I,IF}$  correspond to valleys in  $I$  and vice versa because a cosine function is used as an interrogation function. If a negative cosine interrogation function is used, peaks in the  $\rho_{I,IF}$  would correspond to peaks in  $I$ . Third, some threshold is required below which peaks and valleys are ignored. This threshold eliminates the detection of peaks and valleys in the noise of the correlation, but it can cause some true peaks and valleys to be missed (such as the fourth intensity peak in the current example).

### 3.5 Results

In this section, the fringe-detection algorithm is applied to an interferogram obtained during an actual test. The analysis of this image is used to demonstrate the capabilities of the fringe-detection method when used with experimental data. Note that this image is typical of those taken using oil-film interferometry, and it represents neither

the best possible nor the poorer results often obtained. As in the one-dimensional case, a cosine interrogation fringe is used to analyze this image.

The two-dimensional fringe-detection process is simply an extension of the one-dimensional process described above. Fig. 3.4 shows the steps used to find the peaks and valleys of an interference pattern. First, a windowed region, such as that in Fig. 3.4(a), is extracted from the original image. A two-dimensional autospectral density of the intensity data  $S_{I,I}$  is obtained and is used to determine whether an interrogation fringe is present in the window, and, if so, in what direction the fringe is oriented. Using the frequency and direction information from  $S_{I,I}$ , an interrogation fringe (a negative cosine in this case), such as that shown in Fig. 3.4(b), is constructed. This interrogation fringe is inserted into a large window to ensure that the cross-correlation coefficient drops to zero at the boundaries to simplify later processing. The cross-correlation coefficient  $\rho_{I,IF}$  of the original windowed image and the interrogation fringe is shown in Fig. 3.4(c) as a gray-scale image. In this figure, peaks of  $\rho_{I,IF}$  correspond to the maximas in the original intensity pattern, whereas the  $\rho_{I,IF}$  valleys correspond to intensity minima. Note that the cross-correlation coefficient contains the useful information from the original image, while the noise is eliminated.

The remaining task is to isolate the correlation peaks and valleys and to determine to which locations in the original image they correspond. Contours of constant  $\rho_{i,if}$  are shown in Fig. 3.4(d) where they are overlaid on a gray-scale representation of the correlation coefficient. The white contours represent negative  $\rho_{i,if}$  values, whereas the black contours represent positive contours. The contour separation here is 0.10 with the most positive contours (0.30) lying near the peaks and the most negative contours (-0.30) lying near the valleys. The contours representing  $\rho_{i,if}=0$  have been omitted. To isolate an individual peak, the highest  $\rho_{i,if}$  value in the image is determined. A contour is then drawn around this point at a lower  $\rho_{i,if}$  value ( $\rho_{i,if}=0.20$  is used here) as indicated by the white contours in Fig. 3.4(e). All the points within this contour are eliminated from further consideration, and the process is repeated. Once all peaks above a certain  $\rho_{i,if}$  value ( $\rho_{i,if}=0.30$  is used here) have been found, the process is



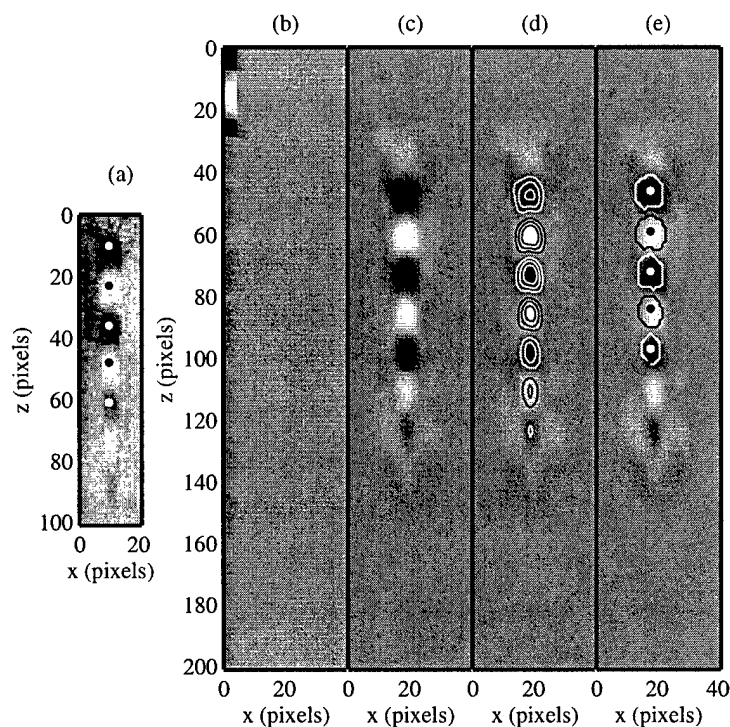


Figure 3.4: Two-dimensional fringe-detection method: (a) windowed area containing a fringe and the location of the peaks and valleys indicated by filled symbols; (b) interrogation fringe, (c) cross-correlation coefficient, (d) cross-correlation coefficient with iso-contours overlaid, (e) cross-correlation coefficient with minima and maxima indicated by symbols and contours used to reject additional peak points shown.

applied to a new window. The isolation of individual valleys is accomplished in a similar manner. The cross-correlation peaks and valleys that are isolated in the cross correlation are indicated by symbols in Fig. 3.4(e), and their corresponding locations in the original image are identified by the symbols in Fig. 3.4(a).

By repeating this process for many windows, interference fringes throughout an image can be identified. The locations of interference fringe peaks and valleys in the experimental image found with fringe detection are shown as stars in Fig. 3.5. In Fig. 3.5(a), a minimum cross-correlation coefficient of 0.30 is specified to be the minimum acceptable fringe peak, and, in Fig. 3.5(b), the minimum is specified to be 0.25. In Fig. 3.5(a), two or more peaks/valleys have been located in approximately 75% of the fringes in this image (this is criteria used here for determining if a fringe has been identified). As important as this is, the low number of spurious locations determine is also important. Note that two of these points are located near a step in intensity, which may yield locally high correlation coefficients. In Fig. 3.5(b), the number of identified fringes increases, but so does the number of spurious locations identified. The results are encouraging in that they have been obtained with a simple cosine interrogation fringe. It is expected that the results will improve with more sophisticated interrogation fringes.

Although this process has been applied to a limited number of data sets, some important observations have been made. Overlapping the windows used to process the data is important to make sure a large portion of the fringe is contained within a window. Multiple fringes in a single window do not appear to affect the results significantly. If not enough of a fringe is present in the window, no dominant frequency in the Fourier transform will be found, and thus it will be ignored. For the results shown in Fig. 3.5, 186 windowed sub-images are analyzed. The windows should also be kept small – just slightly larger than a fringe. This ensures that there is enough energy in the frequency of the intensity autospectral density that is associated with the fringe to identify the window as containing a fringe. Finally, the threshold values used to determine whether a fringe is present and the  $\rho_{i,if}$  thresholds used to determine

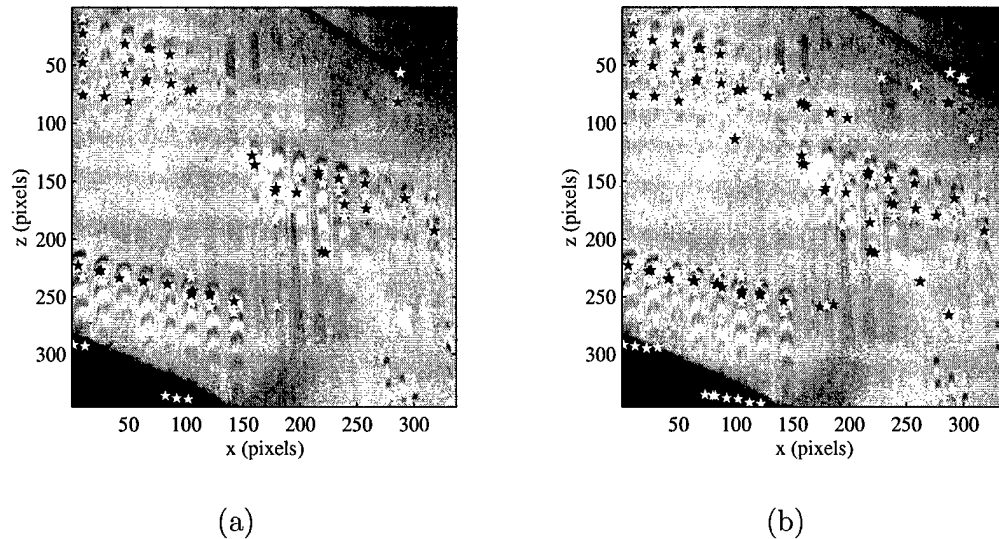


Figure 3.5: Two-dimensional fringe detection applied to an experimental image. The white stars correspond to valleys in the fringe pattern, whereas the black stars correspond to peaks: (a)  $|\rho_{I,IF}| > 0.30$  for a peak or valley, and (b)  $|\rho_{I,IF}| > 0.25$  for a peak or valley.

peak isolation appear to be dependent on the image being considered and the window size used. Therefore, some practice is necessary to determine the combination of these parameters that produces the best results.

### 3.6 Conclusions

A first interference fringe-detection scheme suited for use with oil-film interferometry has been implemented. The scheme uses a combined windowed Fourier transform/correlation approach that allows for the scalability of the interrogation function like a wavelet, without the restrictions imposed on a wavelet. In addition, the two-dimensional case can accommodate fringes at multiple orientations since the interrogation function can be rotated (see reference [8] for details). The cross correlation of these interrogation functions and the original intensity produces a filtered result that isolates the information being sought (i.e. the interference fringe), while much of the noise is eliminated. Although the results are encouraging, improved results are

expected with the use of a more sophisticated interrogation fringe

As developed here, the method has been tailored to fringe detection for oil-film interferometry. This method is general, and it may be applied to isolate any known fringe pattern in an image. For example, this technique could be applied to interferograms used to evaluate optics to scan for specific flaws that produce known changes in the interferogram. Whatever the application, it is important to have a good representation of what it is that is being sought. To this end, improved interrogation fringes for oil-film interferometry are being developed using physically-based interference patterns generated using the thin-oil-film equations and optical relationships.

## Chapter 4

# Modification of Base Pressure Through Boundary Layer Manipulation

### 4.1 Nomenclature

$A_b$	Base Area
$B$	von Karman's Constant, 5.2
$C_{D,fb}$	Integrated Fore-body Drag Coefficient
$C_{D,b}$	Integrated Base Drag Coefficient
$C_{D,p,fb}$	Integrated Fore-body Pressure Drag Coefficient
$C_f$	Skin-Friction Coefficient
$C_{p,fb}$	Fore-body Pressure Coefficient
$C_{p,b}$	Base Pressure Coefficient
$h_b$	Base Height
$k$	Surface Roughness Height
$k^+$	Surface Roughness Height in Wall Units
$L$	Fore-body length

$p_b$	Base Pressure
$p_{fb}$	Fore-body Pressure
$p_{\text{ref}}$	Reference Pressure
$p_\infty$	Free-stream Pressure
$\text{Re}_{\text{ref}}$	Reynolds Number per meter based on $U_{\text{ref}}$
$\text{Re}_{x, \text{ref}}$	Reynolds Number based on $x$ and $U_{\text{ref}}$
$\text{Re}_s$	Reynolds Number based on $s$
$\text{Re}_\theta$	Reynolds Number based on $\theta$
$S_{uu}$	Velocity Auto-spectral Density Function
$s$	Coordinate Along Plate Surface
$u$	Local Stream-wise Velocity
$U_e$	Edge Velocity
$U_\infty$	Free-stream Velocity
$U_{\text{ref}}$	Reference Velocity
$u_\tau$	Friction Velocity
$u^+$	Velocity in Wall Units
$\Delta U^+$	Roughness Shift for Law of the Wake
$W$	Wake function
$x$	Coordinate Parallel to Incoming Flow
$y$	Coordinate Normal to Incoming Flow
$y^+$	Coordinate Normal to Incoming Flow in Wall Units
$y_b$	Shift in $y$ coordinate due to thickness of flat plate model
$y_{\text{offset}}$	$y$ Shift for Rough Boundary Layer
$z$	Span-wise Coordinate
$\delta$	Boundary Layer Thickness
$\delta^*$	Displacement Thickness
$\kappa$	von Karman's Constant, 0.41
$\lambda$	Thwaites Parameter, $\sqrt{2/C_f}$

$\nu$	Kinematic Viscosity
$\Pi$	Coles' Wake Parameter
$\rho$	Density
$\theta$	Momentum Thickness, Ramp Angle
$\tau_w$	Wall Shear Stress

#### Subscripts

$b$	Base
$fb$	Fore-body
ref	Coefficients Based on Reference $U_{\text{ref}}$ and $p_{\text{ref}}$

## 4.2 Introduction

The proposed designs for the next generation of reusable launch vehicles have required large base areas when compared to the overall length of the vehicle. An example of this would be the X-33 reusable launch vehicle demonstrator that requires a large base area in order to employ its linear aero-spike engines. Even though the large base area is necessary for the design of the vehicles, it also means that the vehicles will be dominated by base drag effects upon reentry into the atmosphere. The base drag will be the primary contribution to total vehicle drag due to both the lower base pressures experienced by these vehicles as well as the lower fore-body drag associated with the smaller fore-body area. The increased effect of base drag has many effects on the overall aerodynamic performance of the vehicle, particularly the lift-to-drag (L/D) ratio. As the base drag increases, L/D decreases, which translates directly into an increase in glide slope angle as well as a decrease in cross range and down range. Obviously, an increase in cross range and down range would be desirable so there is flexibility on the reentry point for the vehicle.

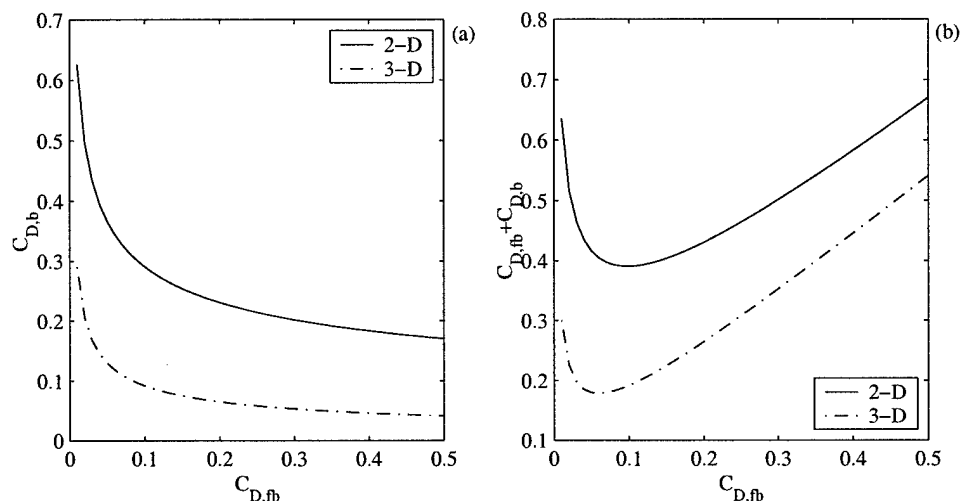


Figure 4.1: Effect of viscous fore-body drag on base drag: (a) relationship between viscous fore-body drag and base drag, (b) “drag bucket” concept.

Work by Hoerner [11], Saltzman *et al.* [23] and Whitmore *et al.* [35] indicates that it is possible to reduce the base drag on these types of vehicles. Hoerner has determined relationships between the viscous fore-body drag and the base drag for both two-dimensional and three-dimensional bodies using data from several bluff bodied vehicle configurations (see Fig. 4.1). Previous vehicle designs with large fore-bodies and small base areas lie on the right-hand side of this curve ( $C_{D,fb} > 0.1$ ). However, the new reusable launch vehicle designs, such as the X-33, lie on the left-hand side of the curves ( $C_{D,fb} < 0.1$ ). From this data, it appears possible that, for certain low values of viscous fore-body drag, an increase in the viscous fore-body drag would decrease the base drag such that the overall drag would be minimized. Fig. 4.1(b) shows that the minimum drag occurs at a specific viscous fore-body drag value. The shape of the curve has been referred to as a “drag bucket” [23].

Hoerner contended that the reduction in base drag from the increased viscous fore-body drag was due to boundary layer isolation. On a surface with a small amount of viscous fore-body drag, a thin boundary layer exists that, upon separation, allows



high momentum fluid from the free-stream to readily mix with the low momentum fluid in the base region. This high rate mixing causes a low base pressure with a high amount of “pumping” of the low momentum fluid. Pumping refers to the acceleration of low momentum fluid using energy from high momentum fluid. As fore-body drag increases, the boundary layer thickens helping to isolate the high momentum fluid from mixing with the low momentum fluid in the base region. As a result, the pressure is higher in the base region (lower pumping), and there is an overall reduction in the base drag.

Another possible explanation that involves vortex dynamics in the wake of the body for the reduction of base drag is presented by Roshko [21]. From studies of bluff bodies with and without splitter plates in the wake, Roshko showed that bodies with splitter plates exhibited higher base pressures with a reduction in the dominant vortex shedding frequency. Studies of wedge flows with and without splitter plates by Tanner [31] showed the same results as Roshko, where the greatest reduction in base drag occurred when the base flow lacked strong vortex shedding. Thus, it is possible that increased fore-body drag may somehow affect the vortex shedding at the base thereby lowering drag.

In order to demonstrate the “drag bucket” concept put forth by Hoerner, the current study investigates the interaction of viscous fore-body drag with base drag on a simple two-dimensional ramp model. Four levels of surface roughness and two base heights are studied. The viscous fore-body drag and base drag are measured in an attempt to replicate the relationship developed by Hoerner. The results are used to determine if surface roughness could be employed to reduce the overall drag of certain types of reusable launch vehicles.

## 4.3 Experimental Approach

In order to vary the test conditions sufficiently so that a wide range of viscous fore-body drag could be generated, a two-dimensional ramp model with two interchangeable ramp angles ( $3^\circ$  and  $5^\circ$ ) has been fabricated. Since the length of the ramp is constant, the base height increases with ramp angle. A consequence of the ramp model is the presence of a favorable pressure gradient on the ramp surface. To vary the viscous fore-body drag, surface roughness has been applied to the model surface. Details of the model and test cases are provided below.

### 4.3.1 2' $\times$ 2' Subsonic Wind Tunnel

This study has been conducted in the University of Wyoming Aeronautics Laboratories (UWAL) 2'  $\times$  2' subsonic wind tunnel. The wind tunnel is a fan-driven, open-return design with a  $0.61 \times 0.61 \times 1.22$  m test section. Using a variable-speed motor, free-stream velocities of 10-50 m/s are possible at a Reynolds number up to  $2.5 \times 10^6/\text{m}$ . The inlet section of the tunnel has a honeycomb insert and three screens located just upstream of a contraction section with a 12:1 ratio. With the current model installed, the measured free-stream turbulence is  $< 0.3\%$ .

### 4.3.2 Ramp Model

In order to demonstrate the relationship between viscous fore-body drag and base drag, a two-dimensional ramp model has been fabricated (Fig. 4.2(a) shows an isometric view of the ramp model and Fig. 4.3 shows the ramp from the side). Two ramp angles ( $3^\circ$  and  $5^\circ$ ) have been implemented to provide a change in the base area. The ramp model has been designed to interface tangent to a point near the leading edge of the existing flat plate model in such a way that a smooth transition occurs. The ramp model has two interchangeable plate locations. Plates used in these locations include a plate fitted with pressure taps to measure the fore-body pressure gradient, a polished stainless steel plate for oil-film interferometry, and plates with various

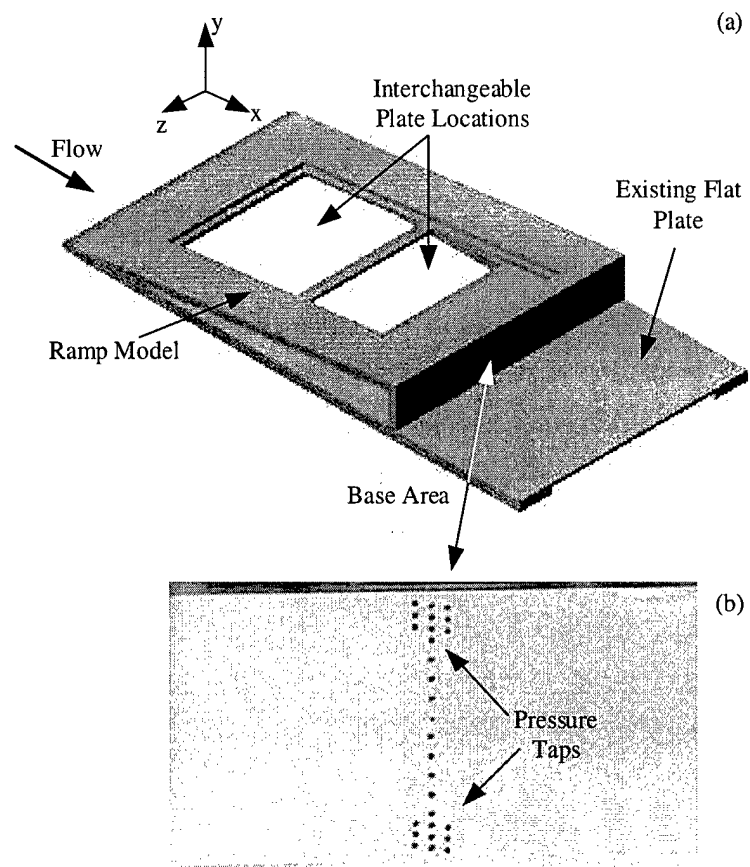


Figure 4.2: View of ramp model: (a) isometric view of assembled model and (b) base area of ramp model.

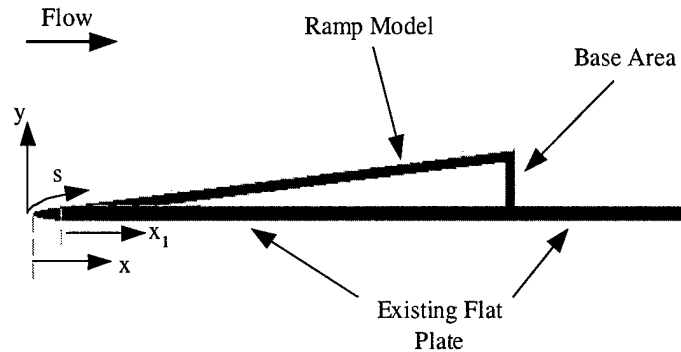


Figure 4.3: Side view of ramp model.

surface roughness. The term fore-body refers to the portion of the model that begins at the tip of the nose and extends to the separation point at the model base.

A body-fitted coordinate system is used in this study as shown in Fig. 4.3. The coordinate along the surface of the model in the stream-wise direction is  $s$ , the coordinate normal to the incoming flow is  $y$ , and the span-wise coordinate is  $z$ . At the base of the model,  $y$  is the coordinate that runs up the base with its origin in the flat plate model.

### 4.3.3 Surface Roughness

Surface roughness is used to modify the boundary layer in order to investigate the effect of fore-body drag on base drag. The purpose of this paper is not to characterize the effects of surface roughness and favorable pressure gradient on the turbulent boundary layers studied here. The reader is referred to Li *et al.* [16] for an in-depth discussion of the boundary layers on the ramps. However, a brief description of surface roughness and its effects is provided below.

Three sizes of silicon sand have been used to generate the surface roughness for this experiment. The sizes of the sand grains are calibrated using mesh screens of a known size. The sorted sand is then applied to the surface of the plates using a

Grain Size Description	k (mm)
Small	0.25
Medium	0.79
Large	2.2

Table 4.1: Sand grain sizes used to produce surface roughness.

spray-on adhesive. Table 4.1 shows the sand grains used in this study.

The effect of roughness on turbulent boundary layers can be partially characterized by  $k^+$ , the roughness expressed in wall units  $k^+ \equiv ku_\tau/\nu$ . There are three roughness regimes for turbulent boundary layer flows: hydraulically smooth, transitionally rough, and fully rough. The hydraulically smooth regime occurs when the surface roughness elements lie within the viscous sublayer ( $k^+ < 5$ ) and the boundary layer velocity profile is equivalent to a profile on a smooth surface. The transitionally rough regime occurs when small perturbations in the surface roughness have a large effect on the boundary layer velocity profile ( $5 < k^+ < 70$ ). The fully rough regime occurs when there is no evidence of the viscous sublayer and the skin friction coefficient becomes independent of  $k^+$  ( $k^+ > 70$ ). Table 4.2 shows the range of values of  $k^+$  found for the two ramp configurations. The small sand grains lie in the transitionally rough regime with an average value of 47 for both the  $3^\circ$  and  $5^\circ$  ramps. The medium and large sand grains lie well within the fully rough regime with average values of 180 and 580, respectively.

#### 4.3.4 Test Cases

In order to characterize the effects of viscous fore-body drag on base drag, several test cases have been run. In order to vary the test conditions sufficiently, three parameters have been changed: base height, roughness and Reynolds number. Two different base heights have been used to study the effect of base to fore-body wetted area. Four levels of roughness are introduced to manipulate the viscous fore-body drag. A range of

Test Condition	$k_{\min}^+ - k_{\max}^+$		
	Small Sand	Medium Sand	Large Sand
3° Ramp $Re_{\text{ref}} = 2.3 \times 10^6$	30– 59	130– 200	470– 650
5 ° Ramp, $Re_{\text{ref}} = 2.1 \times 10^6$	44– 52	150– 230	590– 650

Table 4.2: Range of surface roughness in wall units for two ramp configurations.

Reynolds number has been surveyed by varying the reference velocity. The location for the reference velocity  $U_{\text{ref}}$  and reference pressure  $p_{\text{ref}}$  is arbitrarily chosen at a location near the front of the ramp.

For each test case, several measurements have been made to measure the different types of drag acting on the ramp. To measure viscous fore-body drag, oil-film interferometry is used on smooth surfaces, while hot-wire anemometry is used on both the smooth and rough surfaces. Pressure measurements have been made to determine the fore-body pressure drag, as well as the base drag. Table 4.3 summarizes the cases tested.

## 4.4 Instrumentation

Pressure and shear stress measurements have been required in this test in order to determine the drag on the ramp model. Two methods have been used to determine the shear stress on the fore-body. The first is oil-film interferometry, which is utilized for the smooth surface cases. The second method is hot-wire anemometry, which is used on the smooth and rough surfaces. The fore-body pressure gradient and base pressures have been determined from pressure measurements on the fore-body and the base area, respectively. Table 4.3 indicates the instrumentation that is used in each of the cases tested.

$U_{\text{ref}}$ (m/s)	$Re_{\text{ref}}$ (1/m)	Ramp Angle (deg)	k (mm)	Symbol	Measurement
30.0	$1.5 \times 10^6$	3.0	0.0	+	OFI,BP,FB
40.0	$2.0 \times 10^6$	3.0	0.0	o	OFI,BP,FB
47.0	$2.3 \times 10^6$	3.0	0.0	*	OFI,FB
				•	HWA,BP
47.0	$2.3 \times 10^6$	3.0	0.25	×	HWA,BP
47.0	$2.3 \times 10^6$	3.0	0.79	□	HWA,BP
47.0	$2.3 \times 10^6$	3.0	2.2	◇	HWA,BP
43.0	$2.1 \times 10^6$	5.0	0.0	△	FB
				▽	HWA,BP
43.0	$2.1 \times 10^6$	5.0	0.25	▷	HWA,BP
43.0	$2.1 \times 10^6$	5.0	0.79	◁	HWA,BP
43.0	$2.1 \times 10^6$	5.0	2.2	★	HWA,BP

Table 4.3: Test cases: HWA - hot-wire anemometry, OFI - oil-film interferometry, BP - base pressure, and FB - fore-body pressure. The symbols after each case listing correspond to those in the graphs.

#### 4.4.1 Oil-Film Interferometry

The skin friction on the smooth surfaces is measured using oil-film interferometry. The oil-film interferometry technique relates the thinning rate of oil to the local shear stress imposed in the oil. For a comprehensive review of oil-film interferometry, see Naughton and Sheplak [20]. The specific oil-film interferometry technique used to determine the shear stress in this study is the Fringe Imaging Skin Friction technique (see references [36, 37, 9]).

Oil-film interferometry uses a line or drops of oil on a surface at a location where the skin friction is to be determined. As the oil is exposed to an air flow, it begins to thin. After a short period of time, the oil thickness becomes thin and independent of the initial thickness. The oil is then illuminated by an extended quasi-monochromatic light source. Light reflects from the air-oil and oil-surface interfaces as shown in Fig. 4.4. When recombined, the reflected light causes constructive and destructive

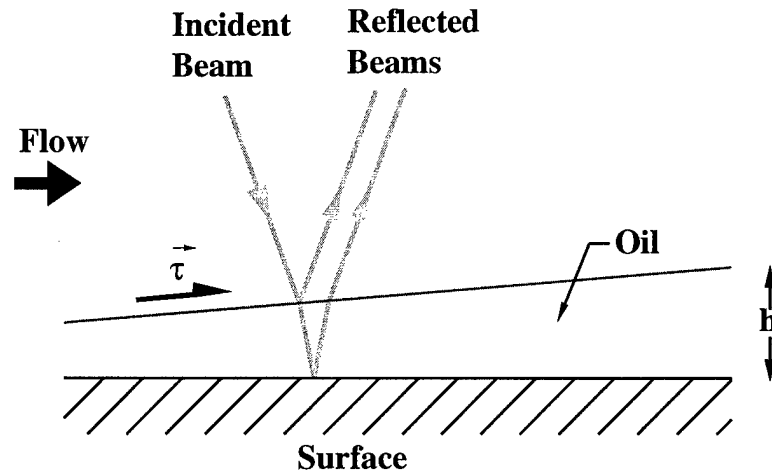


Figure 4.4: Side profile of oil-film “wedge”. Used with permission from [19].

interference depending on the thickness of the oil. The interference patterns are then captured by an imaging device (typically a CCD camera) and are stored on a computer. The height of the oil is related to the spacing of the interference patterns that, with some additional information, can be related to the local shear stress [36]. Fig. 4.5 shows an interferogram typical of those acquired in this study.

#### 4.4.2 Hot-Wire Anemometry

A single wire, constant temperature hot-wire anemometry system is used for these tests. The signal from the anemometer is split in two and sent to a dual channel low-pass filter. The mean hot-wire voltage is determined by DC coupling the first signal and filtering at 10Hz. The fluctuation voltage is AC coupled and filtered at 90% of the Nyquist frequency. The voltages have been converted to velocity using King’s law whose constants are determined in a calibration performed prior to testing. The



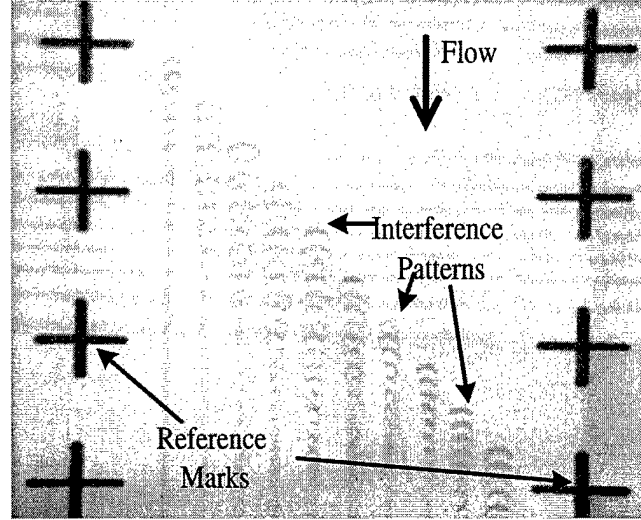


Figure 4.5: Example thin-oil-film interferogram. This interferogram was produced using the oil-drop approach.

temperature is monitored throughout a test, and a temperature correction is applied to the measured values. A typical boundary layer survey contains 50  $y$  locations with 256k points taken at each location at a sampling rate of 10 kHz.

In order to estimate the viscous fore-body drag from the rough surface cases, a function combining the law-of-the-wall for rough surfaces and the law-of-the-wake is used (see reference [33] for details on the individual laws). The resulting wall-wake law for rough surfaces can be expressed as

$$u^+ = \frac{1}{\kappa} \ln(y^+) + B - \Delta U^+ + \frac{2\Pi}{\kappa} W\left(\frac{y}{\delta}\right), \quad (4.1)$$

where

$$W\left(\frac{y}{\delta}\right) \approx \sin^2\left(\frac{\pi y}{2\delta}\right). \quad (4.2)$$

Here  $u^+ \equiv u/u_\tau$  is the velocity in wall units,  $u_\tau \equiv \sqrt{\tau_w/\rho}$  is the friction velocity,  $\kappa$  and  $B$  are von Karman's constants,  $y^+ \equiv (yu_\tau)/\nu$  is the distance from the wall in wall units,  $\Pi$  is Coles wake parameter, and  $\Delta U^+$  is a factor introduced to shift the curve due to the effects of surface roughness. This form of the wall-wake law is also

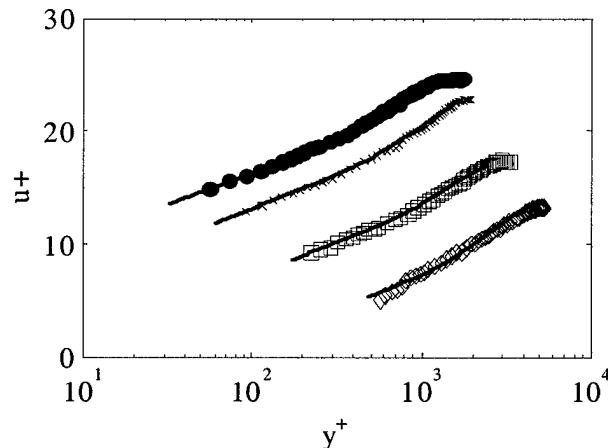


Figure 4.6: Boundary layer profiles at 791 mm from the leading edge for four different roughness values. See Table 4.3 for symbol definitions.

used in reference [12]. A non-linear curve fit of Eq. 4.1 using the hot-wire data ( $u$  and  $y$ ) and a Gauss-Newton method ([14],[17]) is performed for each boundary-layer survey. The results of the non-linear curve fit provides values for  $y_{\text{offset}}$ ,  $u_\tau$ ,  $\Pi$ ,  $\delta$ , and  $\Delta U^+$  (for the rough surface cases). Here,  $y_{\text{offset}}$  was used to shift the location of  $y=0$  since the exact zero location was hard to determine on rough surfaces. Typically, the value of  $y_{\text{offset}}$  is chosen such that the log region of the wall-wake law is satisfied [24]. Using the results of this curve fit, the shear stress (or skin friction) is determined since  $\tau_w = \rho u_\tau^2$ . These values of shear stress are then used to determine the fore-body viscous drag.

Fig. 4.6 shows the results of the non-linear curve fit for the  $3^\circ$  ramp case near the back of the ramp for smooth and rough surfaces. As is evident from the figure, the effect of roughness is to shift the curve downward and to the right. In all cases, the wall-wake law is able to accurately represent the data.

A limited set of hot-wire measurements has also made just downstream of the ramp's base. The record lengths and sampling frequency of these measurements are similar to those for the boundary layer surveys, but there is less spatial resolution in

the wake surveys.

## 4.5 Data Corrections

Much of the data Hoerner compared to the relationship between fore-body and base drag have been acquired from free flight tests. For a valid comparison of the present study with Hoerner's curve, a correction to the wind tunnel data was necessary. Corrections based on standard correction methods for airfoils have proven insufficient, so a more complex approach using simulations of the flow over the model with and without the wind tunnel ceiling was made. The ratio of the results for the two cases, for example  $C_p$  values, provided the appropriate corrections. This level of detail was necessary in this case due the significant blockage this model represents in the wind tunnel. In addition, the simulation provided an appropriate reference pressure and velocity to non-dimensionalize our results with. All of these topics are discussed in greater detail below.

### 4.5.1 Simulation

In order to provide a true wind tunnel correction for the data obtained in this study, a Reynolds-Averaged Navier Stokes Code (OVERFLOW [1]) was used to simulate the flow over the ramp model. For simplicity, the simulations are performed with inviscid wall boundary conditions where walls are present. Two cases have been run for each test condition in the study: the first with the wind tunnel top wall (constrained) and second without the top wall (unconstrained). The unconstrained case is assumed to behave as though the model was exposed to free flight conditions. Simulations have been made over a range of Reynolds numbers near that of the experiment to ensure there is little effect of Reynolds number on the non-dimensional quantities in the flow.

### 4.5.2 Free-Stream Conditions

The ramp model has been designed in such a way that it was impossible to obtain free-stream pressure (and hence free-stream velocity) measurements. Instead a representative reference pressure is used for all pressure measurements. However, the RANS simulations enabled the determination of the free-stream conditions. Pressure measurements are made (using the reference pressure) on the fore-body of the ramp for every ramp angle and velocity condition in the study. From these pressure measurements, the calculated local or edge velocity  $U_{e,m}$  is determined along the length of the ramp using the relationship between pressure and velocity, given by

$$U_{e,m} \frac{dU_{e,m}}{ds} = -\frac{dp}{ds}. \quad (4.3)$$

Next, the calculated local velocity is non-dimensionalized by an assumed free-stream velocity,  $U_{\infty,m}$ . The same approach is applied to the local velocity  $U_{e,s}$  obtained from a simulation with the wind tunnel top wall to obtain a velocity ratio  $U_{e,s}/U_{\infty}$  for the simulation. Finally,  $U_{\infty,m}$  is varied until the best match between the calculated velocity ratio and the velocity ratio from the simulation is obtained in a least square error sense. The resulting  $U_{\infty,m}$  is considered to be the free-stream velocity  $U_{\infty}$  for a particular case. The measured free-stream velocity is then used to calculate the skin-friction coefficient

$$C_{f,m} = \frac{\tau_w}{\frac{1}{2}\rho U_{\infty,m}^2}. \quad (4.4)$$

Once the free-stream velocity is calculated, the pressure data is used to determine the free-stream pressure,  $p_{\infty}$ . The pressure data and  $U_{\infty,s}$  from the simulation are used to determine the simulated pressure coefficient,  $C_{p,s} = (p - p_{\infty})_s / q_{\infty,s}$ , along the length of the ramp. The measured pressures  $p - p_{\text{ref}}$  are adjusted by a factor  $p_{\infty} - p_{\text{ref}}$  and divided by the dynamic pressure to determine the calculated pressure coefficient, defined as

$$C_{p,m} = \frac{(p - p_{\text{ref}}) - (p_{\infty} - p_{\text{ref}})}{q_{\infty}}, \quad (4.5)$$

where  $q_{\infty} = (1/2)\rho U_{\infty}^2$ . The adjustment factor,  $p_{\infty} - p_{\text{ref}}$ , is varied until the best

match between  $C_{p,m}$  and  $C_{p,s}$  is achieved in a least square error sense. The resulting  $p_\infty$  is considered to be the free-stream pressure for a particular case.

### 4.5.3 Blockage Effect

In order to account for the large effect of blockage, two simulations have been made per test condition. The first simulation is made with the wind tunnel top wall (constrained, subscript wt) and the second is made without the top wall (unconstrained, subscript fl). Fore-body pressure coefficients and local velocities are calculated for both cases. Then, at a given location, the ratio of the pressure coefficients,  $C_{p,s,wt}/C_{p,s,fl}$ , is calculated and applied to the measured fore-body pressures to arrive at a corrected fore-body pressure coefficient,

$$C_{p,c} = C_{p,m} \frac{C_{p,s,fl}}{C_{p,s,wt}}. \quad (4.6)$$

A similar process is used to determine the corrected local velocities. The base pressures are corrected for blockage effects by determining the correction factor,  $C_{p,s,wt}/C_{p,s,fl}$ , at the trailing edge of the ramp and applying it to the base pressure data in the same manner as the fore-body pressure data. The subscripts  $c$  and  $m$  will be dropped for the remainder of the paper since all  $C_p$  values discussed are corrected and measured quantities.

The correction for the measured value of  $C_f$  is approached in a slightly different manner. Since the simulations that were run were inviscid, no correction analogous to that applied to the pressure coefficients is possible. The primary effect of the blockage on the shear stress is to accelerate the flow and thus increase the shear stress. However, the shear stress increase should scale with  $U_e^2$ , so the  $C_f$  values are corrected by non-dimensionalizing the wall shear stress by the edge velocity

$$C_{f,c} = C_{f,m} \frac{U_{\infty,m}^2}{U_{e,m}^2}. \quad (4.7)$$

The subscript  $c$  will be dropped for the remainder of the paper since all  $C_f$  values discussed are corrected quantities.

## 4.6 Results

### 4.6.1 Assessment of $C_f$ Measurement Techniques

In order to compare the wall shear stress measurements using hot-wire anemometry and oil-film interferometry with theory, measurements have been made in a smooth, flat plate boundary layer. The skin-friction coefficient  $C_f = 2\tau_w/(\rho U_\infty^2)$  results for this case are shown in Fig. 4.7 as a function of the Reynolds number based on the momentum thickness  $Re_\theta$ . Two sets of data are shown: the oil-film-interferometry (OFI) results and hot-wire anemometry (HWA) results. In addition, the momentum integral relationship between  $C_f$  and  $Re_\theta$

$$Re_\theta = \lambda \left( \frac{3.75}{\lambda} - \frac{24.778}{\lambda^2} \right) e^{0.4(\lambda-8)}, \quad (4.8)$$

where  $\lambda = \sqrt{2/C_f}$ , is also shown [32]. Good agreement is demonstrated between the oil-film interferometry results and the momentum integral results. It should be noted that the hot-wire anemometry results are consistently above the momentum integral results at lower Reynolds numbers. This is most likely attributed to the use of the wall-wake fit to calculate  $\tau_w$ . For low values of  $Re_\theta$ , the boundary layer may not have been fully turbulent, and thus Eq. 4.1 does not strictly apply. Nonetheless, the measurements shown in Fig. 4.7 can be used to assess the approximate accuracy of hot-wire anemometry for shear stress measurement.

### 4.6.2 Integral Boundary Layer Properties

A detailed characterization of the effect of roughness and favorable pressure gradient on the boundary layer was carried out by Li *et al.* [16]. For this experiment, only the momentum thickness,  $\theta$ , and the displacement thickness,  $\delta^*$ , at the trailing edge of the ramp are used to characterize the modification of the boundary layer caused by the roughness. The displacement thickness is defined as

$$\delta^* = \int_0^\infty \left( 1 - \frac{u}{U_e} \right) dy. \quad (4.9)$$

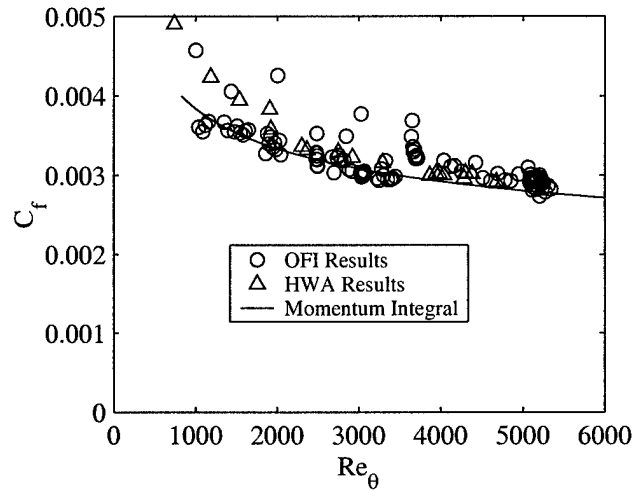


Figure 4.7: Skin-friction coefficient for smooth flat plate,  $U_\infty=50$  m/s. Used with permission from [15].

Correspondingly, the momentum thickness is defined as

$$\theta = \int_0^\infty \frac{u}{U_e} \left(1 - \frac{u}{U_e}\right) dy. \quad (4.10)$$

Table 4.4 shows the displacement and momentum thicknesses at the trailing edge of the ramp for a number of cases. It can be seen that roughness increases the displacement and momentum thicknesses by a maximum factor of 2.5 for the 3° ramp. Correspondingly, the displacement and momentum thicknesses are increased by an order of magnitude for the 5° ramp. The drastic increases for the 5° ramp are due, in part, to the presence of a transitional boundary layer on the smooth surface ramp that produces an extremely thin boundary layer.

### 4.6.3 Skin-Friction Results

The viscous fore-body shear stress distribution has been determined for the 3° and 5° ramps using oil-film interferometry and hot-wire anemometry. The results of these measurements are shown in Fig. 4.6.3(a) for the 3° ramp and in Fig. 4.6.3(b) for the

$\text{Re}_{\text{ref}}$	$U_{\text{ref}}$ (m/s)	Ramp Angle (deg)	k (mm)	$\delta^*$ (mm)	$\theta$ (mm)
$2.3 \times 10^6$	47	3.0	0.0	1.43	1.12
$2.3 \times 10^6$	47	3.0	0.25	2.05	1.57
$2.3 \times 10^6$	47	3.0	0.79	2.58	1.92
$2.3 \times 10^6$	47	3.0	2.2	4.00	2.69
$2.1 \times 10^6$	43	5.0	0.0	0.39	0.23
$2.1 \times 10^6$	43	5.0	0.25	2.22	1.55
$2.1 \times 10^6$	43	5.0	0.79	2.87	1.95
$2.1 \times 10^6$	43	5.0	2.2	3.49	2.32

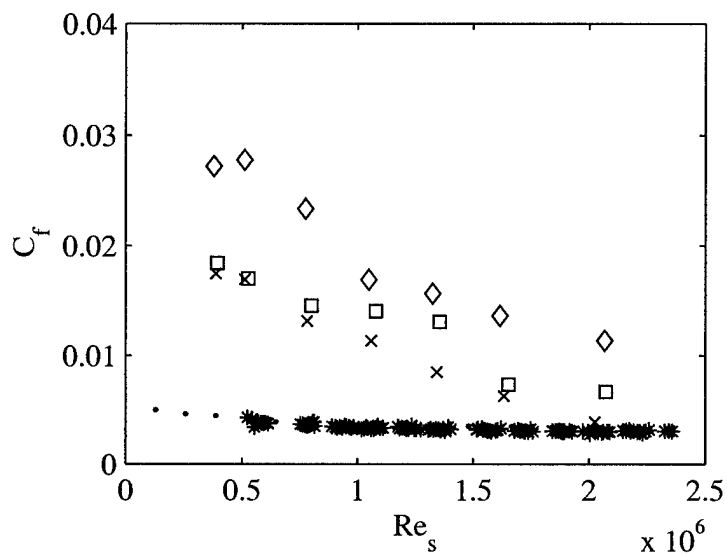
Table 4.4: Integral boundary layer properties near the trailing edge of the ramp for various test conditions. Used with permission from [15].

5° ramp. In the figure, it is observed that, as expected, the skin friction increases with an increase in roughness height. The largest roughness increases  $C_{f,\text{ref}}$  on the 3° ramp by a factor of six over the smooth case. Smooth surface shear stress is not available for the 5° ramp because the resulting boundary layer is not fully turbulent, which prevents the hot-wire data from being accurately represented by the wall-wake curve fit. Another interesting observation is that the skin-friction coefficient continues to increase even after the surface is fully rough. This is most likely due to the fact that the effect of roughness is modified by the presence of the pressure gradient on the fore-body. The typical uncertainty in the wall shear stress is  $\approx 5\text{-}10\%$  for the oil-film interferometry measurements and  $\approx 10\text{-}20\%$  for the hot-wire anemometry measurements.

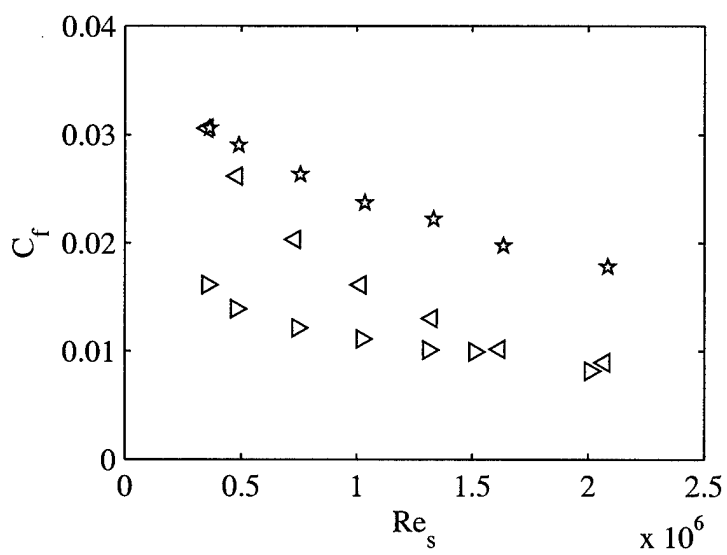
#### 4.6.4 Fore-Body Pressure Results

The fore-body pressure results (subscript  $fb$ ) are shown in Fig. 4.9 for all cases in the study. The fore-body pressure gradient for the three 3° cases collapse to the same trend ( $-0.14 < C_{p,fb} < -0.20$ ), while the 5° case exhibited an increased favorable pressure gradient ( $-0.14 < C_{p,fb} < -0.25$ ) as expected. A slight negative pressure





(a)



(b)

Figure 4.8: Skin-friction coefficient: (a) 3 degree ramp with  $U_\infty=47.4$  m/s and (b) 5 degree ramp with  $U_\infty=40.7$  m/s. See Table 4.3 for symbol definitions. Rough surface data used with permission from [15].

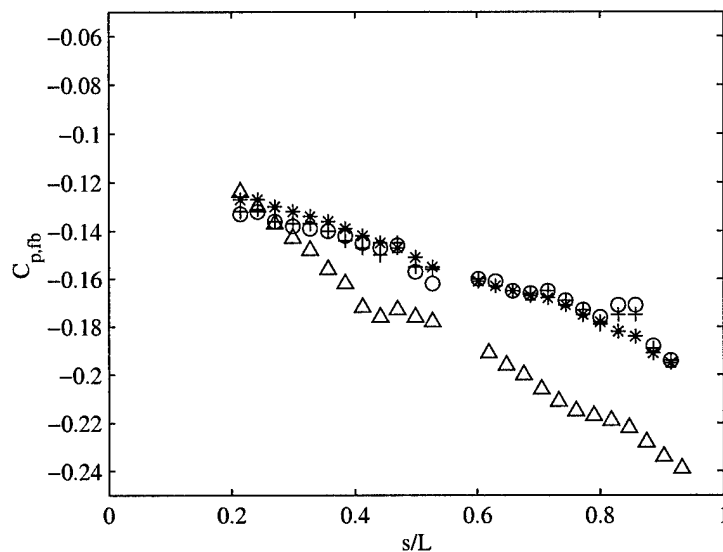


Figure 4.9: Fore-body pressure coefficient for the ramp cases. See Table 4.3 for symbol definitions.

coefficient is expected as the typical value for this type of model (except a region near the nose of the model). The uncertainty in the fore-body pressure coefficient is  $\approx 1\%$ . Since the fore-body pressure coefficients are negative and act on the forward facing portion of the ramp, its contribution to pressure drag will be in the opposite direction of the base pressure drag.

#### 4.6.5 Base Pressure Results

The base pressure coefficients  $C_{p,b}$  are shown in Fig. 4.10. It should be noted from this figure that, for a given ramp angle, the base pressure remains fairly constant (to within the accuracy of the calculation) with an increase in fore-body surface roughness. This is especially true for the  $5^\circ$  case where the different surface roughnesses collapse to the same base pressure coefficient. The uncertainty in the base pressure coefficient is  $\approx 1\%$ . These results contrast with those of Whitmore *et al.* [35] in which a measurable increase in base pressure was found with increasing roughness.

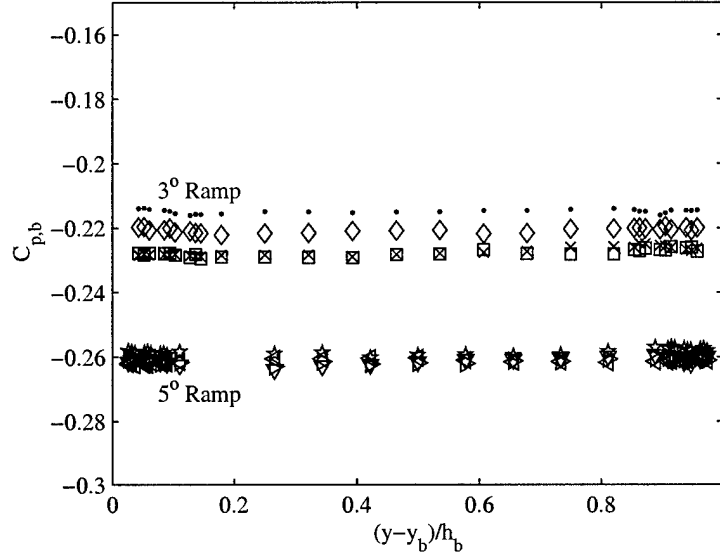


Figure 4.10: Coefficient of pressure for ramp base area: 3° ramp at  $U_\infty = 47.4$  m/s and 5° ramp at  $U_\infty = 40.7$  m/s. See Table 4.3 for symbol definitions.

#### 4.6.6 Integrated Results

In order to validate the relationship between viscous fore-body drag and base drag developed by Hoerner, the pressure and shear stress distributions must be integrated. If the pressures are assumed to be independent of span-wise location  $z$ , the integrated base drag is given by

$$C_{D,b} = w \int_{y_b}^{h_b} \frac{p_b - p_\infty}{\frac{1}{2} \rho U_\infty^2 A_b} dy, \quad (4.11)$$

whereas the integrated viscous fore-body drag is

$$C_{D,fb} = w \int_{x_1}^L \frac{\tau_w \cos \theta}{\frac{1}{2} \rho U_\infty^2 A_b} ds, \quad (4.12)$$

where  $\theta$  is the ramp angle,  $A_b = (w \times h_b)$  is the area of the base, and  $x_1$  is the location where the ramp model interfaces with the flat plate model (see Fig. 4.3). It should be noted that both integrated drag quantities use the same reference velocity and are non-dimensionalized by the *base* area in accordance with Hoerner's approach [11].

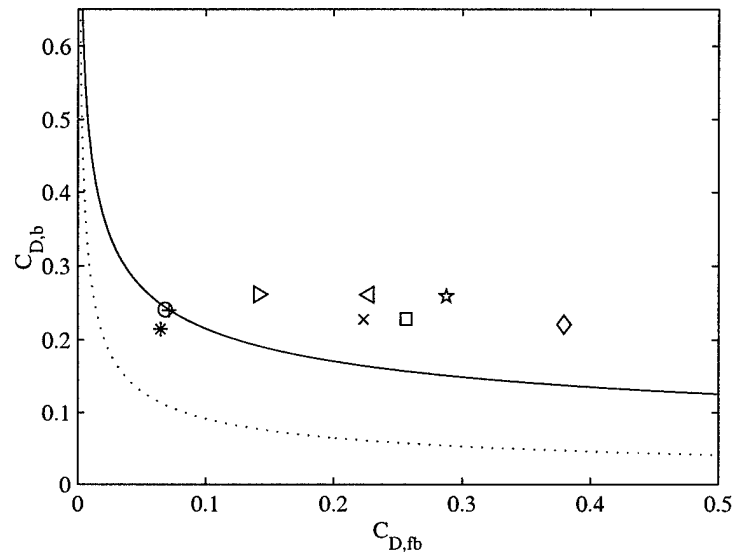


Figure 4.11: Effect of viscous fore-body drag on base drag. See Table 4.3 for symbol definitions. The solid line represents Hoerner's 2-D surface imperfections (i.e. sheet metal junctions) curve and the dotted line represents Hoerner's 3-D curve.

All integrations were accomplished using a trapezoidal method. A plot of  $C_{D,b}$  versus  $C_{D,fb}$  is shown in Fig. 4.11.

From this graph, two important observations should be noted. First, there is no obvious effect of roughness on base drag such as that seen in the experiments of Whitmore *et al.* [35]. Second, the values of  $C_{D,b}$  and  $C_{D,fb}$  are fairly constant for the case where the Reynolds number was varied from  $1.5 \times 10^6$  to  $2.3 \times 10^6$  for the smooth  $3^\circ$  ramp (the three points to the far left in the figure) indicating an insensitivity to Reynolds number over this range.

As shown in Fig. 4.9, a substantial favorable fore-body pressure gradient exists for the cases presented in this study. This contrasts with the free-flight data points used by Hoerner, which had very small fore-body pressure gradients. As a result of the lower  $C_p$  values on the ramp upstream of the base, the base drag will be higher than for a fore-body with little or no pressure gradient on it. Therefore, for these flows

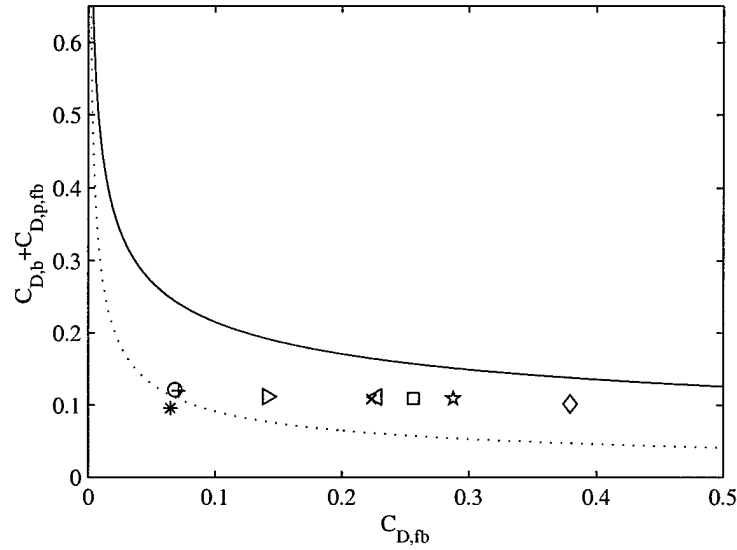


Figure 4.12: Effect of viscous fore-body drag on total pressure drag. See Table 4.3 for symbol definitions. The solid line represents Hoerner's 2-D surface imperfections (i.e. sheet metal junctions) curve and the dotted line represents Hoerner's 3-D curve.

with high pressure gradients on the fore-body, including the effects of the fore-body drag helps to calculate a base drag that is more representative of the flow in the base region and not due to the effects on the fore-body. The integrated fore-body pressure drag is given by

$$C_{D,p,fb} = w \int_{x_1}^L \frac{(p_{fb} - p_{\infty}) \sin \theta}{\frac{1}{2} \rho U_{\infty}^2 A_b} ds. \quad (4.13)$$

Here, the variables are the same as those defined above for the integrated base and viscous drag. The impact of including the fore-body pressure drag is shown in Fig. 4.12. The overall trend of the data is the same as in Fig. 4.10, where an increase in viscous fore-body drag has little effect on the total pressure drag and a Reynolds number invariance is noticed for the 3° smooth cases.

### 4.6.7 Wake Measurements

In order to examine the role of vortex dynamics in the base drag observed here, hot-wire velocity measurements have been made in the wake of the ramp model. The auto-spectral density of the velocity at a point in the wake of the  $3^\circ$  base at approximately the base height is shown in Fig. 4.13. In this figure, no dominant frequency is evident, which can be interpreted as indicating that there is no dominant vortex shedding frequency.

It is believed that the absence of vortex shedding may have been caused by the model surface downstream of the base area, which, as discussed previously, is known to impede vortex dynamics (see Roshko [21] and Tanner [31]). However, this observation may also be due to high levels of fore-body drag present here.

### 4.6.8 Discussion

Three of the results from this study are important and require further discussion here. First, it is noted that an increase in viscous fore-body drag (a factor of 6 increase for the  $3^\circ$  ramp) has very little effect on the base drag. Even though the boundary layer is thickened considerably, there is no noticeable decrease in base drag. There are several possible explanations for this result. The first is that the model surface downstream of the base area is acting as a long splitter plate and has already lowered the base drag over what it would be if the body had no such model surface. A second explanation is that the fore-body drag is so large on this model that additional fore-body drag has little effect (see Fig. 4.1).

The second important result is that there is no evidence of a dominant frequency in the wake as would be expected if periodic vortex shedding is playing a large role in the base drag observed here. This result suggests that a critical phenomena responsible for base drag may have been suppressed by the model used here.

The final important result is the deviation of the data obtained in this study to that of Hoerner's curves. The data from the study is flat in a region where Hoerner's curves still have a bit of curvature and lies between the 2-D surface imperfections

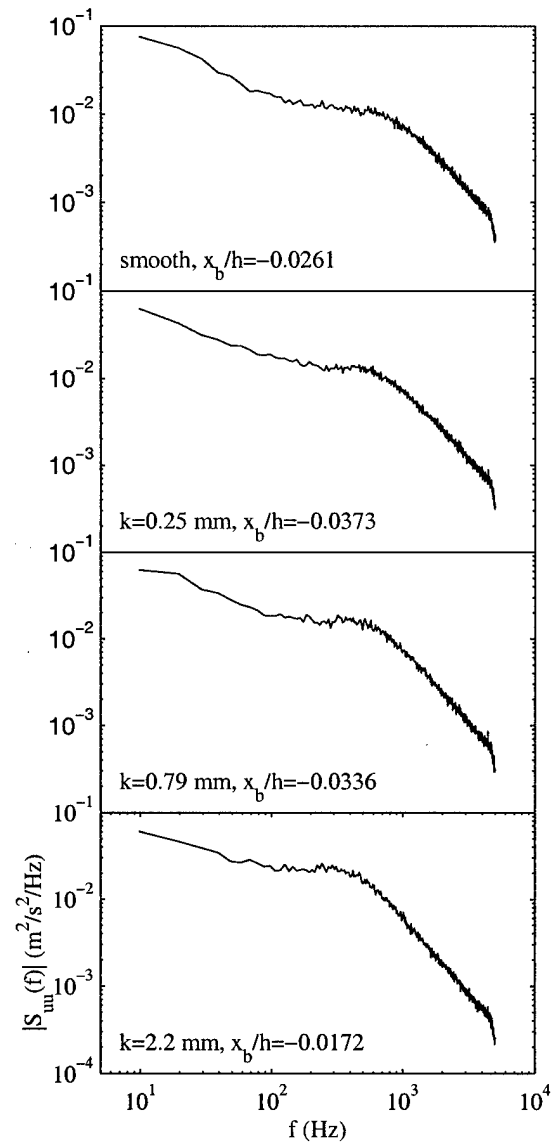


Figure 4.13: Auto-spectral density of fluctuating velocities measured at a location  $x/h = 0.59$  behind the  $3^\circ$  ramp at  $U_{\text{ref}} = 47$  m/s.

curve and the 3-D bodies curve. These deviations could likely arise from the 2-D ramp model used in this study is not like any of the bodies studied by Hoerner. Another possible explanation is that the contribution of viscous fore-body drag and fore-body pressure drag from the nose of the model have been neglected (the model prevented the measurement of these quantities). It should also be noted that an increase in viscous fore-body increased the total drag of the model (which moved the total drag points away from the minimum point in the “drag bucket”).

## 4.7 Conclusion

The potential use of viscous fore-body drag to reduce base drag has been considered in this study. Detailed pressure, shear stress, and boundary-layer measurements have been carried out. The results of these measurements show that, for the two-dimensional ramp model used in this study, an increase in viscous fore-body drag has very little effect on the base drag. For example, the viscous fore-body drag is increased by a factor of 6 but no appreciable change is noticed in the base drag. This contrasts results of an experiment by Whitmore *et al.* [35], which suggest that an increase in viscous fore-body drag would reduce base drag.

Additionally, the results of the study show that a simple thickening of the boundary layer does not seem to change the base drag, which contrasts Hoerner's theory. Even though a substantial increase in the boundary layer thickness is observed ( $\approx 3\times$  for the  $3^\circ$  ramp and  $\approx 10\times$  for the  $5^\circ$  ramp) the base drag remains fairly constant. This means that Hoerner's simple jet pumping mechanism is not the sole effect responsible for base drag reduction in this type of geometry. Hot-wire measurements in the wake of the model show that the flow in the base region is devoid of a dominant shedding frequency. It may be possible that the boundary layer somehow affects the vortex shedding mechanism but further investigations would be necessary to demonstrate that this is true.

At this point it appears that using roughness to decrease base drag is inconclusive



since the behavior of the model used in this study is much different than expected. Additional experiments should be conducted on a full wedge model before a final determination is made about the use of surface roughness to reduce base drag.

## Chapter 5

### Conclusions

In this study, two important topics were developed. The first was the development of an automation procedure used in conjunction with the oil-film interferometry technique. The second was to study the effect of modifying viscous fore-body drag on base drag. Each of these topics will be summarized in greater detail below.

A new automation procedure was developed for use with the oil-film interferometry measurements used in this experiment. The technique used a combined windowed Fourier transform and a correlation function to determine regions in the interferogram where oil-film fringes are likely to reside. The cross correlation of a single cycle cosine function and the original intensity produced a filtered result that isolated the information being sought, while eliminating much of the noise. Additional work should focus on developing new interrogation functions (instead of the single cycle cosine function) that more accurately represent the oil-film interference patterns.

The effect of viscous fore-body drag on base drag was investigated. Oil-film interferometry and hot-wire anemometry were used to determine the viscous fore-body drag, while measurements of pressure in the base area provided the base drag. The results of the study showed that an increase in viscous fore-body drag had very little effect on the base drag, which is in contrast with a previous study by Whitmore *et al.* [35]. This also contrasts the data presented by Hoerner, which predicted that an increase in viscous fore-body drag (and thus a thickening of the boundary layer)

would tend to decrease the base drag. As a result it would not be possible to decrease base drag by using surface roughness for this model geometry. Another important observation is that the model surface downstream of the base area has introduced from the flat plate on the ramp model has impeded the vortex dynamics in the base region of the ramp model. This vortex impeding effect suggests that a new model is required to increase understanding about the interaction of the boundary layer state and vortex shedding with base drag. Future base drag reduction work should focus on a true three-dimensional wind tunnel model. Careful surveys of the boundary layer, as well as the wake should be made to understand the interaction between boundary layer state and vortex shedding frequency. The wind tunnel model should be constructed in such a way as to allow for easy measurement of a true reference pressure and velocity.

# Bibliography

- [1] *OVERFLOW User's Manual*, February 1998. Version 1.8.
- [2] *Matlab Image Processing Toolkit*, third edition, June 2001.
- [3] J. Bendat and A. Piersol. *Random Data: Analysis and Measurement Procedures*. John Wiley & Sons, New York, NY, 1986.
- [4] L. Cattafesta III and J. Moore. Review and Application of Non-photographic Photogrammetry to Quantitative Flow Visualization. AIAA Paper 96-2180, June 1996.
- [5] L. Clancy. *Aerodynamics*. Halsted Press, 1975.
- [6] H. Coleman and W. Steele Jr. *Experimentation and Uncertainty Analysis for Engineers*. John Wiley and Sons, 1st edition, 1989.
- [7] R. Decker and J. Naughton. Improved Fringe Imaging Skin Friction Analysis Using Automated Fringe Identification. AIAA Paper 2001-0557, January 2001.
- [8] R. Decker, J. Naughton, and F. Jafari. Automatic Fringe Detection for Oil Film Interferometric Skin-Friction Measurement. In I. Grant and G. Carlomagno, editors, *Proceedings of the 9th International Symposium on Flow Visualization*, 2000. (on CD ROM, ISBN 0 9533991 1 7).
- [9] D. Driver. Application of Oil Film Interferometry Skin-Friction to Large Wind Tunnels. In *81st AGARD Fluid Dynamics Panel Meeting & Symposium*, Sept. 22-25, Seattle WA, 1997.

- [10] T. Garrison and M. Ackman. Development of a Global Interferometer Skin-Friction Meter. *AIAA Journal*, 36(1):62–68, January 1998.
- [11] S. Hoerner. *Fluid Dynamic Drag*. Self-published, 1965.
- [12] P. Krogstad and R. Antonia. Surface Roughness Effects in Turbulent Boundary Layers. *Experiments in Fluids*, 27:450–460, 1999.
- [13] H. Kurzweg. Interrelationship Between Boundary Layer and Base Pressure. *Journal of the Aeronautical Sciences*, pages 743–748, 1951.
- [14] K. Levenberg. A Method for the Solution of Certain Problems in Least Squares. *Quarterly of Applied Mathematics*, 2:164–168, 1944.
- [15] W. Li. Characteristics of Turbulent Boundary Layers on Rough Surfaces with Favorable Pressure Gradients. Master's thesis, University of Wyoming, Laramie, WY, August 2001.
- [16] W. Li, R. Decker, J. Lew, J. Naughton, and S. Whitmore. Characteristics of Turbulent Boundary Layers on Rough Surfaces with Favorable Pressure Gradients. AIAA Paper 2001-2915, June 2001.
- [17] D. Marquardt. An Algorithm for Least-Squares Estimation of Nonlinear Parameters. *SIAM Journal of Applied Mathematics*, 11:431–441, 1963.
- [18] D. Monson and G. Mateer. Boundary-Layer Transition and Global Skin Friction Measurements with an Oil-Fringe Imaging Technique. In *SAE 932550, Aerotech '93, Costa Mesa, CA, Sept. 27–30*. Society of Automotive Engineers, 1993.
- [19] J. Naughton and J. Brown. Surface Interferometric Skin-Friction Measurement Technique. AIAA Paper 96-2183, June 1996.
- [20] J. Naughton and M. Sheplak. Modern Skin Friction Measurement Techniques: Description, Use, and What to do with the Data. AIAA Paper 2000-2521, June 2000.

- [21] A. Roshko. On the Drag and Shedding Frequency of Two-Dimensional Bluff Bodies. Technical report, NACA TN 3169, July 1954.
- [22] A. Rowe, A. Fry, and F. Motallebi. Influence of Boundary-Layer Thickness on Base Pressure and Vortex Shedding Frequency. *AIAA Journal*, 39(4):754–756, 2000.
- [23] E. Saltzman, K. Wang, and K. Iliff. Flight-Determined Subsonic Lift and Drag Characteristics of Seven Lifting-Body and Wing-Body Reentry Vehicle Configurations with Truncated Bases. AIAA Paper 99-0383, January 1999.
- [24] H. Schlichting and K. Gersten. *Boundary-Layer Theory*. Springer, 2000.
- [25] J. Seto and H. Hornung. Internally mounted thin-liquid-film skin-friction meter - Comparison with floating element method with and without pressure gradient. AIAA Paper 91-0060, January 1991.
- [26] J. Seto and H. Hornung. Two-Directional Skin Friction Measurement Utilizing a Compact Internally-Mounted Thin-Liquid-Film Skin Friction Meter. AIAA Paper 93-0180, January 1993.
- [27] L. Squire. The Motion of a Thin Oil Sheet Under the Boundary Layer on a Body. In R.L. Maltby, editor, *Flow Visualization in Wind Tunnels Using Indicators*, AGARDograph 70, pages 7–23. 1962.
- [28] M. Takeda, I. Hideki, and S. Kobayashi. Fourier-Transform Method of Fringe-Pattern Analysis for Computer-Based Topography and Interferometry. *Journal of the Optical Society of America*, 72(1), January 1982.
- [29] L. Tanner. Skin Friction Measurement by Viscosity Balance in Air and Water Flows. *Journal of Physics E: Scientific Instruments*, 12:610–19, 1979.
- [30] L. Tanner and L. Blows. A Study of the Motion of Oil Films on Surfaces in Air Flow, with Application to the Measurement of Skin Friction. *Journal of Physics E: Scientific Measurements*, 9(3):194–202, 1976.

- [31] M. Tanner. Reduction of Base Drag. *Prog. Aerospace Sci.*, 16(4):369–384, 1975.
- [32] F. White. *Viscous Fluid Flow*. McGraw-Hill, 1st edition, 1974.
- [33] F. White. *Viscous Fluid Flow*. McGraw-Hill, 2nd edition, 1991.
- [34] S. Whitmore and T. Moes. A Base Drag Reduction Experiment on the X-33 Linear Aerospike SR-71 Experiment (LASRE) Flight Program. AIAA Paper 99-0277, January 1999.
- [35] S. Whitmore, S. Sprague, and J. Naughton. Wind-tunnel Investigations of Blunt-body Drag Reduction Using Forebody Surface Roughness. AIAA Paper 2001-0252, January 2001.
- [36] G. Zilliac. Further Developments of the Fringe-Imaging Skin Friction Technique. Technical report, NASA TM 110425, December 1996.
- [37] G. Zilliac. The Fringe-Imaging Skin Friction Technique PC Application User's Manual. Technical report, NASA TM 1999-208794, 1999.

# Appendix A

## Uncertainty Analysis

For the study presented here, two different methods of calculating uncertainty were employed: the first involves calculating the uncertainty of a measurement and the second involves the uncertainty of a calculation. The uncertainty of a measurement can be further broken into two parts: bias errors and precision errors. The bias error is a fixed error whose value is the same for every measurement taken with the same device. The precision error is a random error whose value changes for every measurement taken with the same device. For additional information about the uncertainty analysis presented here, see [6].

### A.1 Density Uncertainty

Air density,  $\rho$ , is calculated using

$$\rho = \frac{P_{\text{atm}}}{RT_{\text{atm}}}, \quad (\text{A.1})$$

where  $R$ , the gas constant for air, is 286.9 J/(kg K) and is assumed to have negligible uncertainty. The uncertainty in the atmospheric pressure measurement,  $U_{P_{\text{atm}}}$ , is 0.01 in. Hg (33.86 Pa) and the uncertainty in the atmospheric temperature measurement,  $U_{T_{\text{atm}}}$ , is 1 K. The uncertainty in the air density calculation is defined by

$$U_{\rho}^2 = \left( \frac{1}{RT_{\text{atm}}} \right)^2 (U_{P_{\text{atm}}})^2 + \left( -\frac{P_{\text{atm}}}{RT_{\text{atm}}^2} \right)^2 (U_{T_{\text{atm}}})^2, \quad (\text{A.2})$$



or as an uncertainty ratio by

$$\left(\frac{U_\rho}{\rho}\right)^2 = \left(\frac{U_{P_{\text{atm}}}}{P_{\text{atm}}}\right)^2 + \left(\frac{U_{T_{\text{atm}}}}{T_{\text{atm}}}\right)^2, \quad (\text{A.3})$$

which results in a typical air density uncertainty ratio,  $U_\rho/\rho$ , of 0.35%.

## A.2 Pitot Static Pressure Uncertainty

The pitot static pressure measurements include the effects of both bias and precision errors. The uncertainty in the pitot static pressure measurements was quantified using

$$U_{\Delta p}^2 = B_{\Delta p}^2 + P_{\Delta p}^2, \quad (\text{A.4})$$

where  $B_{\Delta p}$  is the bias error of the pressure transducer and  $P_{\Delta p}$  is the precision error of the measurements. The bias error in the pressure transducers is very small ( $\approx 4 \times 10^{-6}$  Pa) when compared to the precision errors, and is therefore neglected. The precision error is calculated (with a 95% confidence level) using

$$P_{\Delta p} = \frac{2\Delta p_{\text{rms}}}{\sqrt{N}}. \quad (\text{A.5})$$

Here  $N$  is the number of samples ( $N=1000$  for all cases in this study) and  $\Delta p_{\text{rms}}$  is the standard deviation of the pressure readings. The resulting pitot static pressure uncertainty ratio,  $U_{\Delta p}/\Delta p$ , is  $\approx 1.8\text{-}7.0\%$ .

## A.3 Free-Stream Velocity Uncertainty

The free-stream velocity,  $V$ , is calculated from the measured pitot static pressure difference using

$$V = \sqrt{\frac{2\Delta p}{\rho}}. \quad (\text{A.6})$$

The uncertainty in the free-stream velocity calculation is given by

$$U_V^2 = \left(\frac{1}{\sqrt{2\Delta p\rho}}\right)^2 (U_{\Delta p})^2 + \left(\sqrt{\frac{\Delta p}{2\rho^3}}\right)^2 (U_\rho)^2, \quad (\text{A.7})$$

or as an uncertainty ratio by

$$\left(\frac{U_V}{V}\right)^2 = \frac{1}{4} \left(\frac{U_\rho}{\rho}\right)^2 + \frac{1}{4} \left(\frac{U_{\Delta p}}{\Delta p}\right)^2. \quad (\text{A.8})$$

The analysis results in a typical free-stream velocity uncertainty ratio,  $U_V/V$ , of  $\approx 0.9\text{-}3.5\%$ .

## A.4 Base Pressure Uncertainty

The base pressure measurements include the effects of both bias and precision errors. The uncertainty in the base pressure measurements was quantified using

$$U_{\Delta p_b}^2 = B_{\Delta p_b}^2 + P_{\Delta p_b}^2, \quad (\text{A.9})$$

where  $B_{\Delta p_b}$  is the bias error of the pressure transducer and  $P_{\Delta p_b}$  is the precision error of the measurements. The bias error in the pressure transducers is assumed to be much smaller than the precision error since the transducers were zeroed before ever run, and is therefore neglected. The precision error is calculated (with a 95% confidence level) using

$$P_{\Delta p_b} = \frac{2\Delta p_{\text{rms}}}{\sqrt{N}}. \quad (\text{A.10})$$

Here  $N$  is the number of samples ( $N=1000$  for all cases in this study) and  $\Delta p_{\text{rms}}$  is the standard deviation of the pressure readings. Table A.1 shows the results of the base pressure measurement uncertainty analysis for the cases run in this study.

## A.5 Pressure Coefficient Uncertainty

The pressure coefficient is defined as

$$C_p = \frac{2\Delta p}{\rho U_{\text{ref}}^2}. \quad (\text{A.11})$$

From this definition of the pressure coefficient, the uncertainty in this calculation is defined as

$$U_{C_p}^2 = \left(\frac{2}{\rho U_{\text{ref}}^2}\right)^2 (U_{\Delta p})^2 + \left(-\frac{\Delta p}{\rho^2 U_{\text{ref}}^2}\right)^2 (U_\rho)^2 + \left(-\frac{2\Delta p}{3\rho U_{\text{ref}}^3}\right)^2 (U_{U_{\text{ref}}})^2, \quad (\text{A.12})$$

Ramp Angle (deg)	$U_{\text{ref}}$ (m/s)	$k$ (mm)	$U_{\Delta p_b}$ (Pa)	$\frac{U_{\Delta p_b}}{\Delta p_b}$
3	30	0.0	1.99	1.10%
3	40	0.0	2.08	0.66%
3	47	0.0	2.94	0.64%
3	47	0.25	2.89	0.58%
3	47	0.8	3.03	0.60%
3	47	2.2	2.82	0.59%
5	43	0.0	3.53	0.58%
5	43	0.25	3.51	0.58%
5	43	0.8	3.63	0.59%
5	43	2.2	3.55	0.59%

Table A.1: Base pressure measurement uncertainty.

or as an uncertainty ratio

$$\left(\frac{U_{C_p}}{C_p}\right)^2 = \left(\frac{U_\rho}{\rho}\right)^2 + \left(\frac{U_{\Delta p}}{\Delta p}\right)^2 + 4 \left(\frac{U_{U_{\text{ref}}}}{U_{\text{ref}}}\right)^2. \quad (\text{A.13})$$

The results of the uncertainty analysis for the pressure coefficient are shown in Table A.2.

## A.6 Skin Friction Uncertainty

### A.6.1 Hot-Wire Anemometry

A numerical uncertainty analysis was used to quantify the uncertainty of the wall shear stress calculated by the non-linear curve fit of the hot-wire data. A random number generator was used to produce velocities bounded by the 95% confidence level. The non-linear curve fit of the wall-wake law was repeatedly applied to the random velocities to determine the uncertainty of the skin friction velocity,  $u_\tau$ . The results of this analysis yield that  $U_{u_\tau}/u_\tau \approx 5\text{-}10\%$  (for more details about the skin

Ramp Angle (deg)	$U_{\text{ref}}$ (m/s)	$k$ (mm)	$U_{C_p}$	$\frac{U_{C_p}}{C_p}$
3	47	0.0	0.0039	0.86%
3	47	0.25	0.0039	0.82%
3	47	0.8	0.0040	0.84%
3	47	2.2	0.0038	0.83%
5	43	0.0	0.0061	0.80%
5	43	0.25	0.0061	0.80%
5	43	0.8	0.0062	0.81%
5	43	2.2	0.0061	0.81%

Table A.2: Pressure coefficient uncertainty.

friction velocity analysis, see [15]). The wall shear stress is defined from the skin friction velocity as

$$\tau_w = \rho u_\tau^2. \quad (\text{A.14})$$

From this definition for the wall shear stress, it is possible to develop the wall shear stress uncertainty ratio as

$$\left( \frac{U_{\tau_w}}{\tau_w} \right)^2 = \left( \frac{U_\rho}{\rho} \right)^2 + 4 \left( \frac{U_{u_\tau}}{u_\tau} \right)^2, \quad (\text{A.15})$$

with typical values of  $U_{\tau_w}/\tau_w \approx 10\text{-}20\%$ .

# Appendix B

## Detailed Derivations

### B.1 Oil Calibration

The measured value of viscosity was calculated using the following steps. The two efflux times were multiplied by their corresponding time constants (these are dependent upon the tube number, in this case for tube 6  $B_{const} = 0.02$  poise/sec and  $C_{const} = 0.006$  poise/sec). This gives two values for the dynamic viscosity in poise. The dynamic viscosity is averaged and divided by the density, then multiplied by  $1 \times 10^5$  to obtain the kinematic viscosity in cSt. The following example shows the calculation of the kinematic viscosity for the 10cSt oil.

$$\text{Efflux Time (sec)} \times \text{Efflux Constant (poise/sec)} = \text{Dynamic Viscosity (poise)}$$

$$5.3 \text{ sec} \times 0.02 \text{ poise/sec} = 0.106 \text{ poise}$$

$$22.8 \text{ sec} \times 0.006 \text{ poise/sec} = 0.1368 \text{ poise}$$

$$\frac{\text{Average Dynamic Viscosity (poise)}}{\text{Density (kg/m}^3\text{)}} \times (1 \times 10^5) = \text{Kinematic Viscosity (cSt)}$$

$$\frac{0.1214 \text{ poise}}{935 \text{ kg/m}^3} \times (1 \times 10^5) = 12.98 \text{ cSt}$$

<b>Trade Name</b>	<b>Nominal Viscosity cSt</b>	<b>Tube Number</b>	<b>Efflux Time, Bulb B sec</b>	<b>Efflux Time, Bulb C sec</b>
Dow 200 Fluid	10	6	5.3	22.8
Dow 200 Fluid	50	6	27.2	91.1
Dow 200 Fluid	100	6	50.7	167.9

Table B.1: Properties measured during viscosity calibration.